CANCER IMMUNOLOGY

Copyright © 2024 The Authors, some rights reserved; exclusive licensee American Association for the Advancement of Science. No claim to original U.S. Government Works

Response to tumor-infiltrating lymphocyte adoptive therapy is associated with preexisting CD8$^+$ T-myeloid cell networks in melanoma

David Barras[1,2]†, Eleonora Ghisoni[1,2,3]†, Johanna Chiffelle[1,2]†, Angela Orcurto[2,3], Julien Dagher[4], Noémie Fahr[1], Fabrizio Benedetti[1], Isaac Crespo[1], Alizée J. Grimm[1], Matteo Morotti[1], Stefan Zimmermann[2,3], Rafael Duran[5], Martina Imbimbo[2,3], Maria Ochoa de Olza[2,3], Blanca Navarro[2,3], Krisztian Homicsko[1,2,3], Sara Bobisse[1,2], Danny Labes[6], Zoe Tsourti[7], Charitini Andriakopoulou[7], Fernanda Herrera[1,8], Rémy Pétremand[1,2], Reinhard Dummer[9], Gregoire Berthod[10], Anne I. Kraemer[1,2], Florian Huber[1,2], Jonathan Thevenet[2,11], Michal Bassani-Sternberg[1,2], Niklaus Schaefer[12], John O. Prior[12], Maurice Matter[13], Veronica Aedo[10], Clarisse Dromain[5], Jesus Corria-Osorio[1,2], Stéphanie Tissot[2,11], Lana E. Kandalaft[1,2,11], Raphael Gottardo[1,14], Mikaël Pittet[1,15], Christine Sempoux[4], Olivier Michielin[1,10], Urania Dafni[16], Lionel Trueb[2,3], Alexandre Harari[1,2], Denarda Dangaj Laniti[1,2]*‡, George Coukos[1,2,3]*‡

Adoptive cell therapy (ACT) using ex vivo–expanded tumor-infiltrating lymphocytes (TILs) can eliminate or shrink metastatic melanoma, but its long-term efficacy remains limited to a fraction of patients. Using longitudinal samples from 13 patients with metastatic melanoma treated with TIL-ACT in a phase 1 clinical study, we interrogated cellular states within the tumor microenvironment (TME) and their interactions. We performed bulk and single-cell RNA sequencing, whole-exome sequencing, and spatial proteomic analyses in pre- and post-ACT tumor tissues, finding that ACT responders exhibited higher basal tumor cell–intrinsic immunogenicity and mutational burden. Compared with nonresponders, CD8$^+$ TILs exhibited increased cytotoxicity, exhaustion, and costimulation, whereas myeloid cells had increased type I interferon signaling in responders. Cell-cell interaction prediction analyses corroborated by spatial neighborhood analyses revealed that responders had rich baseline intratumoral and stromal tumor–reactive T cell networks with activated myeloid populations. Successful TIL-ACT therapy further reprogrammed the myeloid compartment and increased TIL-myeloid networks. Our systematic target discovery study identifies potential T-myeloid cell network–based biomarkers that could improve patient selection and guide the design of ACT clinical trials.

INTRODUCTION

Adoptive cell therapy (ACT) using ex vivo–expanded autologous tumor-infiltrating lymphocytes (TILs) is a potent cancer therapeutic approach, with objective responses seen in a subset of patients with metastatic melanoma in multiple clinical studies (*1*–*3*), and is superior to immune checkpoint blockade (ICB) therapy in these patients (*4*, *5*). Clinical responses with TIL-ACT have also been reported in other epithelial cancers (*6*–*8*); however, the benefit of TIL-ACT does not extend to all treated patients for reasons that remain unclear.

Advances in single-cell technologies have enabled in-depth characterization of tumor and immune cells in the tumor microenvironment (TME). Although the molecular profiles of CD4$^+$ and CD8$^+$ tumor-specific TILs at the steady state have been recently reported by single-cell RNA sequencing (scRNA-seq) (*9*–*11*), the features of other leukocytes regulating T cell function or performance during ACT remain unclear. Understanding the steady-state immune contexture could help improve the selection or preconditioning of patients receiving TIL-ACT. Furthermore, understanding the dynamics of the human solid tumor TME during TIL-ACT may elucidate key mechanisms supporting T cell–mediated tumor rejection and therapeutic resistance as well as guide future therapeutic strategies.

To identify the states of T cells and other cells in the TME associated with successful TIL-ACT, we carried out scRNA-seq and bulk RNA-seq and multispectral immunofluorescence (mIF) imaging

Downloaded from https://www.science.org at University of Lausanne on February 05, 2024

---

[1]Ludwig Institute for Cancer Research, Lausanne Branch, Department of Oncology, University of Lausanne (UNIL) and Lausanne University Hospital (CHUV), Agora Cancer Research Center, Lausanne, Switzerland. [2]Center for Cell Therapy, CHUV-Ludwig Institute, Lausanne, Switzerland. [3]Service of Immuno-oncology, Department of Oncology, Lausanne University Hospital, Lausanne, Switzerland. [4]Unit of Translational Oncopathology, Institute of Pathology, Lausanne University Hospital, Lausanne, Switzerland. [5]Department of Radiology and Interventional Radiology, Lausanne University Hospital, Lausanne, Switzerland. [6]Flow Cytometry Facility, Department of Formation and Research, University of Lausanne, Epalinges, Switzerland. [7]Scientific Research Consulting Hellas, Athens, Greece. [8]Service of Radiation Oncology, Department of Oncology, Lausanne University Hospital, Lausanne, Switzerland. [9]Department of Dermatology, University Hospital Zurich, Zurich, Switzerland. [10]Department of Oncology, Lausanne University Hospital (CHUV), Lausanne, Switzerland. [11]Department of Oncology, Center of Experimental Therapeutics, Lausanne University Hospital (CHUV) and University of Lausanne (UNIL), Lausanne, Switzerland. [12]Department of Nuclear Medicine and Molecular Imaging, Lausanne University Hospital, Lausanne, Switzerland. [13]Department of Visceral Surgery, Lausanne University Hospital, and University of Lausanne, Lausannne, Switzerland. [14]Biomedical Data Science Center and Swiss Institute of Bioinformatics, Faculty of Biology and Medicine, University of Lausanne, Lausanne, Switzerland. [15]Department of Pathology and Immunology, University of Geneva, Geneva, Switzerland. [16]Faculty of Nursing, National and Kapodistrian University of Athens, Athens, Greece.
*Corresponding author. Email: george.coukos@chuv.ch (G.C.); denarda.dangaj@chuv.ch (D.D.L.)
†These authors contributed equally to this work.
‡These authors contributed equally to this work.

analysis of longitudinal samples from patients with metastatic melanoma before and after TIL-ACT in a phase 1 clinical study (NCT03475134). We show that clinical responses of melanoma to TIL-ACT are associated with preexisting and identifiable CD8$^+$ TIL-myeloid cell networks, which support tumor immune attack at the steady state and reorganize TILs after ACT to sustain tumor rejection.

RESULTS

Steady-state melanoma microenvironment of patients receiving TIL-ACT

We analyzed 13 patients with metastatic melanoma who received TIL-ACT after progression on ICB therapies (data file S1) from the total of 15 enrolled in a phase 1 clinical study (NCT03475134) between March 2018 and December 2020. Patients received ex vivo–expanded TILs (*12*) and bolus intravenous interleukin-2 (IL-2) support after non-myeloablative lymphodepletion chemotherapy, according to established protocols (Fig. 1A) (*2*). We observed objective responses [best overall response according to response evaluation criteria in solid tumors (RECIST) criteria v.1.1] in six patients [46%, classified as responders (Rs)]: Two patients attained an ongoing complete response (CR) and four patients had a partial response (PR). Non-Rs (NRs) included four patients with progressive disease (PD) and three patients with stable disease (SD) (two with SD only on the first post-enrollment tumor assessment, ~6 weeks after enrollment, and one with durable SD up to 10 months) (Fig. 1B). Among the 13 patients, the median progression-free survival (PFS) was 5.6 months [95% confidence interval (CI), 1.2 to 8.5], with a median follow-up of 45.4 months [interquartile range (IQR), 40.9 to 50.3]; the median overall survival (OS) was 8.8 months (95% CI, 7.5 to not reached) (Fig. 1C). The two CR patients had mono-ICB therapy, whereas the four PR (transient Rs) and six of seven NR patients had dual ICB therapy before their enrollment. In univariate analyses, none of neutrophil-to-lymphocyte ratio, v-raf murine sarcoma viral oncogene homolog B1 (BRAF) V600E/K mutational status, sum of targeted lesions or three-dimensional (3D) tumor volume, presence of brain metastases, and lactate dehydrogenase levels significantly associated with PFS or OS (data file S1). Gender was the only parameter that significantly correlated with PFS but not OS.

To understand the baseline cellular landscape of these tumors, we interrogated 12 available surgical samples from 10 patients (6 Rs and 4 NRs) by scRNA-seq (fig. S1A). We found that cells distributed into 21 major clusters, including T cells, B cells, myeloid cells, and other stroma and vascular endothelial cells (Fig. 1D and fig. S2, A to C). Nonmalignant cell populations segregated in the uniform manifold approximation and projection (UMAP) space, with cells from different patients intermixed (fig. S2A). Using the TCGA (the Cancer Genome Atlas), we built a melanoma cell–specific gene signature score and identified 59,958 tumor cells. Tumor cells from different patients clustered separately, indicating high patient specificity (Fig. 1D and fig. S2, A and D). We found no differences in malignant cell and immune cell proportions based on clinical response. Although NRs exhibited a trend of lower total TILs, this was with high interpatient variability (Fig. 1E).

Baseline melanomas of Rs exhibit tumor-intrinsic immunogenicity

We then interrogated the baseline malignant compartment (Fig. 2A). Compared with TME host cells, melanoma cells exhibited evident chromosomal copy number variation (CNV) inferred from single-cell gene expression (*13*). This finding validated the malignant nature and suggested genomic instability of melanoma cells (Fig. 2B). By interrogating several copy number thresholds for both deletion and amplification, we observed that Rs overall exhibited more copy number deletions, both at gene and segment levels, suggestive of higher genomic instability, albeit these differences were not statistically different for all thresholds examined (fig. S2, E and F).

To further dissect differences in malignant cells between Rs and NRs, we conducted transcriptomic analyses. Single-cell regulatory network inference and clustering (SCENIC) analysis, which infers transcription factor (TF) activity based on regulon (TF and its target genes) expression (*14*), revealed several signal transducers and activators of transcription (STATs) and interferon (IFN) regulatory factors (IRFs) among the top activated regulons in melanoma cells of Rs (Fig. 2C). This finding was associated with an enrichment of well-differentiated predominantly epithelioid SRY-Box transcription factor 10 (SOX10)$^+$ melanoma cells in Rs compared with that in NRs (fig. S2G), in agreement with recent findings demonstrating that the loss of SOX10 expression leads to invasive properties through the expression of mesenchymal and extracellular matrix genes (*15*). Moreover, single-sample gene set enrichment analysis showed activation of immunogenic programs in melanoma cells from Rs, including double-stranded DNA sensing, IFN-α and IFN-γ responses, complement activation, antigen presentation, major histocompatibility complex (MHC) class I/II, IL-6/Janus kinase/STAT3 signaling, tumor necrosis factor–α/nuclear factor κB (NF-κB) signaling, and immune checkpoints (Fig. 2, D and E, and fig. S2, H and I). In agreement, we found higher expressions of *B2M*; *TAP1*; *HLA-E*, *-A*, and *-C*; *PSMB8*; and *PSMB9*, encoding MHC class I/II antigen presentation components and immunoproteasome activation, in tumor cells from Rs (Fig. 2F and data file S2).

The increased antigen presentation observed in tumor cells from Rs prompted us to explore whether these cells had a higher tumor mutational burden (TMB). Through whole-exome sequencing analyses conducted in tumors and, when feasible, in autologous tumor-derived cell lines, we found that Rs displayed a greater number of somatic mutations compared with NRs (Fig. 2G and data file S3). To validate these results, we classified the TCGA metastatic melanoma cohort according to our cohort's malignant-cell ACT clinical response signature (Fig. 2F) and found that the TCGA melanoma samples having high levels of this signature also had higher TMBs (Fig. 2H).

To search for melanoma-intrinsic programs associated with the lack of response to TIL-ACT, we interrogated a broader collection of reactome signatures and found the mesenchymal epithelial transition (MET)–driven phosphatidylinositol 3-kinase (PI3K)–AKT pathway as the only significantly overexpressed program in melanoma cells of NRs (Fig. 2I and data file S4). We also found higher, albeit not significantly, pathways associated with cellular proliferation, such as resolution of D-loop structures, DNA replication initiation, and G_1- and G_2-related programs, which are suggestive of DNA repair competence (Fig. 2, D and I, and data file S4). In summary, Rs exhibit higher TMB along with increased immunogenic activation and antigen presentation.

Melanomas responding to TIL-ACT exhibit preexisting CD8$^+$ T cell immunity

We next examined the T cell compartment in baseline tumors. The proportions of overall CD4$^+$ TILs, CD8$^+$ TILs, and CD45$^+$

Downloaded from https://www.science.org at University of Lausanne on February 05, 2024

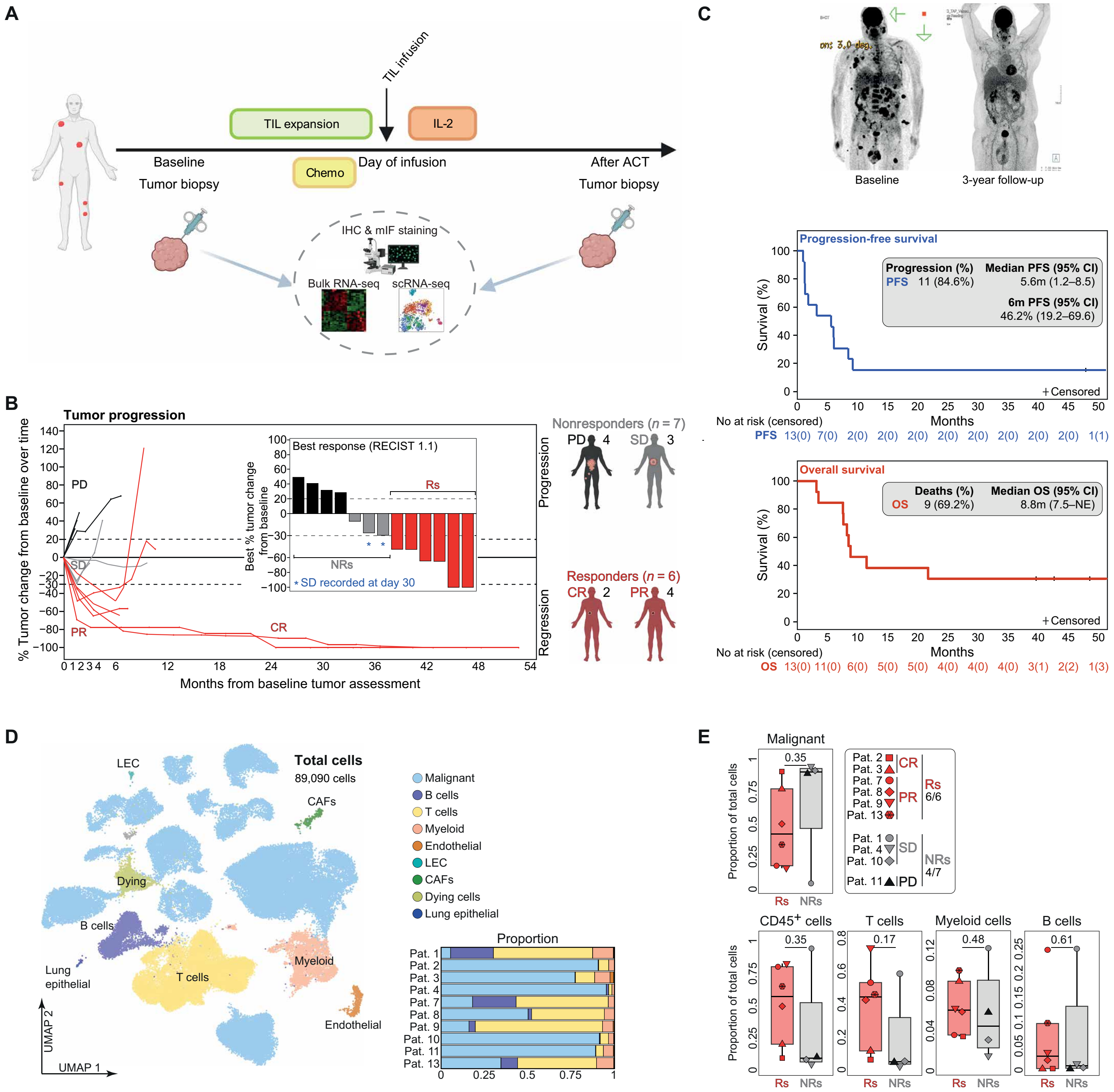

Fig. 1. Clinical characteristics and TME landscape of the melanoma TIL-ACT cohort. (**A**) Schematic representation of the study design and time points for translational analysis. (**B**) Spider plot showing percentage of tumor size change relative to baseline over time. The inset shows the best tumor size change (%) in sum of target lesions from the baseline. (**C**) Positron emission tomography–computed tomography (PET-CT) images of patient #3 (who had CR) at baseline and at 3 years follow-up (top) and PFS (middle) and OS (bottom) of the studied cohort (NCT03475134) by Kaplan-Meier method. NE, not estimable. (**D**) UMAP projection of scRNA-seq data from 10 baseline melanoma highlighting the main cell–type populations and their proportions. Pat., patient. CAFs, cancer-associated fibroblasts. LEC, lymphatic endothelial cells. (**E**) Box plots showing main cell–type proportions according to clinical response. Statistical significance was assessed using Wilcoxon rank sum test comparing Rs versus NRs.

leukocytes were not significantly different between Rs and NRs (Fig. 1E and fig. S3A). By scRNA-seq performed on sorted CD45$^+$ cells from all 13 patients, we identified nine different CD8$^+$ TIL clusters. We assigned these clusters on the basis of prior knowledge (*9*, *16*–*19*) to known states (Fig. 3, A and B; fig. S3, B and C; and data file S5), including naive-like, effector memory (EM)–like, *CX3CR1*$^+$, heat-shock gene-positive, *FOXP3*$^+$, IFN-stimulated gene (ISG)–positive, precursor exhausted (P$_{ex}$), and exhausted (T$_{ex}$). In addition, we identified natural killer (NK)–like CD8$^+$ TILs, a NK cell cluster, and three CD4$^+$ T cell subsets: T helper 1 (T$_H$1), *CXCL13*$^+$ T

Downloaded from https://www.science.org at University of Lausanne on February 05, 2024

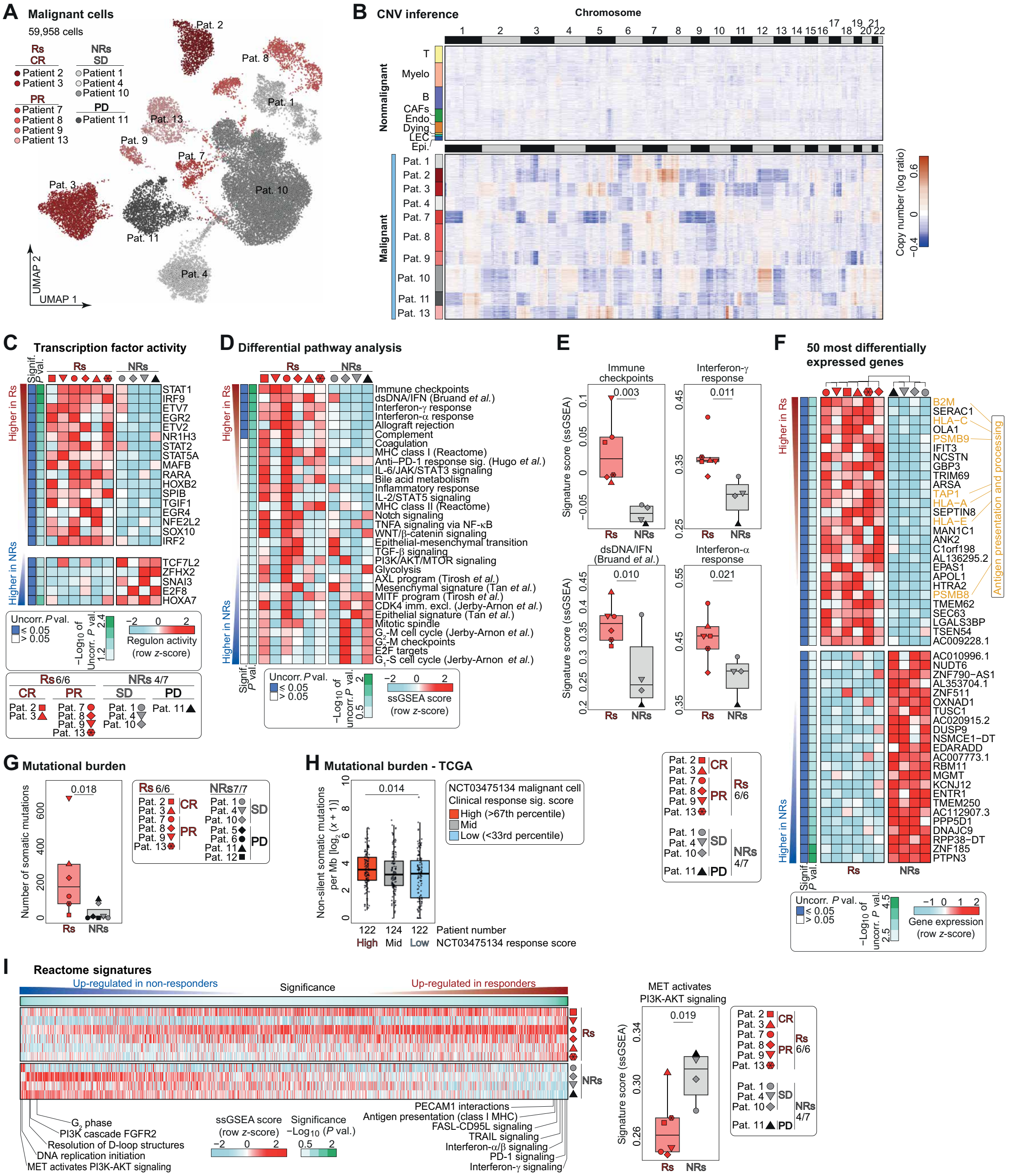

Fig. 2. The baseline malignant compartment of Rs is characterized by high immunogenicity and mutational burden. (**A**) UMAP projection of malignant cells from 10 baseline melanoma. (**B**) CNV inferred from gene expression of 200 randomly selected melanoma cells per patient. Similar results of nonmalignant cells are given as reference at the top. (**C**) Heatmap showing the most significant (unadjusted $P < 0.05$) activated and repressed TF/regulon in malignant cells from Rs versus NRs. (**D**) Heatmap of hallmarks and curated pathways that are the most differentially represented between malignant cells of Rs and NRs. dsDNA, double-stranded DNA; TGF-β, transforming growth factor–β; JAK, Janus kinase. (**E**) Box plots showing malignant cell signature scores appearing in (D) according to clinical response. Statistical significance was extracted from linear regression analysis performed in (D). ssGSEA, single-sample gene set enrichment analysis. (**F**) Heatmap showing clustering of the most up- and down-regulated significant (unadjusted $P < 0.05$) genes in malignant cells from Rs versus NRs. Genes belonging to the antigen presentation and processing pathway are highlighted in yellow. (**G**) Box plot showing the number of somatic mutations computed from whole-exome sequencing data of tumors or cell lines according to clinical response. (**H**) Box plot showing the number of non-silent somatic mutations per megabase in the TCGA metastatic melanoma cases ($n = 368$) according to our malignant clinical signature levels (high, mid, and low). (**I**) Left: Reactome pathway analysis showing selected pathways that are the most differentially represented between malignant cells from Rs and NRs. Right: Box plot showing the most significant malignant cell signature scores up-regulated in NRs. Patient–pseudo-bulk–averaged values of malignant cells are shown (C to F and I). Statistical significances were assessed using linear regression (C to F and I) or Wilcoxon rank sum test (G and H). PECAM1, platelet endothelial cell adhesion molecule 1. TNFA, tumor necrosis factor alpha. AXL, AXL receptor tyrosine kinase. MTOR, mechanistic target of rapamycin. FASL, Fas ligand. TRAIL, TNF-related apoptosis-inducing ligand.

Downloaded from https://www.science.org at University of Lausanne on February 05, 2024

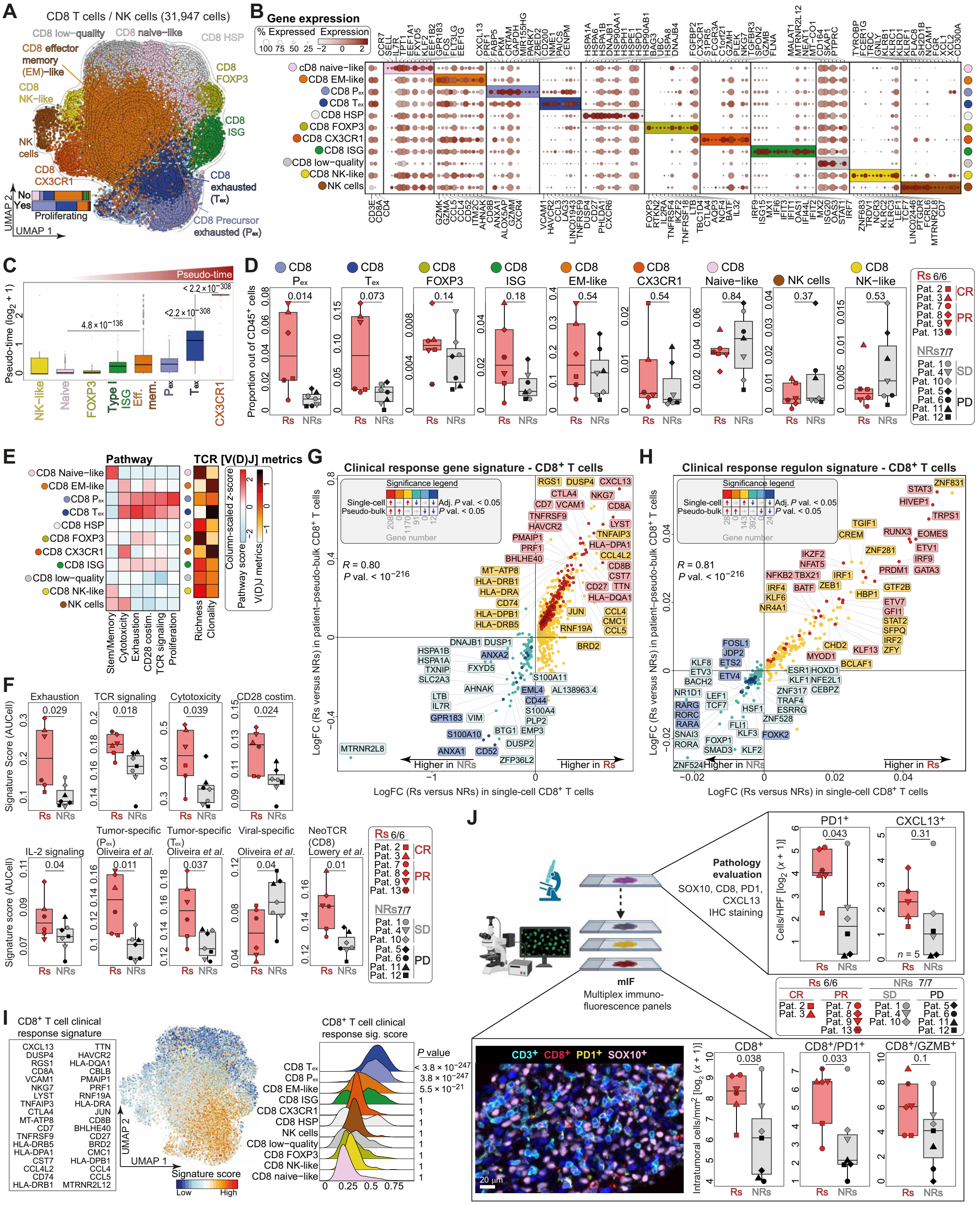

Fig. 3. CD8$^+$ T cells from tumors of ACT Rs exhibit hallmarks of antitumor immunity at baseline. (**A**) UMAP projection showing subclustering of CD8$^+$ T and NK cells from CD45$^+$ cell–sorted data of 13 baseline and 7 post-ACT tumors. (**B**) Dot plot showing gene expression of most discriminant gene markers for CD8$^+$ T cell populations. (**C**) Pseudo-time analysis of the CD8$^+$ T cell populations showing pseudo-time values per cell grouped per CD8$^+$ T cell subtype. (**D**) Box plots of CD8$^+$ T cell subtypes and NK cell proportions over CD45$^+$ cells in baseline tumors according to clinical response. (**E**) Left: Gene signature score–averaged pseudo-bulk per CD8$^+$ T cell population. Right: TCR richness and clonality metrics per CD8$^+$ T cell population. (**F**) Box plots of patient-averaged CD8$^+$ T cell pseudo-bulk signature scores according to clinical response in baseline tumors. (**G** and **H**) Differential gene expression (G) and TF/regulon (H) analysis between CD8$^+$ T cells from Rs versus NRs in baseline tumors at single-cell (*x* axis) and patient–pseudo-bulk (*y* axis) levels. (**I**) CD8$^+$ T cell clinical response gene signature (left) and its scoring projected in UMAP space (middle) and plotted as ridge plot per CD8$^+$ T cell subsets in baseline tumors. (**J**) Pathological evaluation by IHC (top right) and mIF (image example at the bottom) quantification in baseline tumors for the indicated proteins. Statistical significances were assessed using one-way ANOVA followed by post hoc Tukey test (C), Wilcoxon rank sum test (D and F), linear regression (G and H), two-sided Student's *t* test (J), or Bonferroni-adjusted one-sided Student's *t* test (I).

Downloaded from https://www.science.org at University of Lausanne on February 05, 2024

follicular helper (T_{FH})–like, and T regulatory (T_{reg}) cells (fig. S3, D and E, and data file S5). State phenotypic divergence of $CD8^+$ TILs inferred by pseudo-time differentiation trajectories suggested that *CX3CR1*$^+$, P_{ex}, and T_{ex} (and a fraction of ISG and EM-like) $CD8^+$ TILs were the most differentiated effector states but represented distinct programs (Fig. 3C and fig. S4A). These three states together contributed to one-third of all $CD8^+$ TILs recovered, whereas EM-like cells contributed another third (Fig. 3D).

Recently, human tumor antigen–specific $CD8^+$ TILs were found to distribute across three *TOX*$^+$*PDCD1*$^+$*CTLA4*$^+$*TIGIT*$^+$ transcriptional exhaustion states, including a precursor state (high expression of *TCF7*, *LEF1*, *CCR7*, and *IL7R*), a terminally differentiated state [high *HAVCR2*/T cell immunoglobulin and mucin-domain containing-3 (TIM3) and *ENTPD1*/CD39 and cytolytic effector molecules], and an intermediate state defined by TFs of recent T cell receptor (TCR) engagement. Here, we found a significant enrichment of P_{ex} and a nearly significant enrichment of T_{ex} $CD8^+$ TILs in Rs (Fig. 3D). Consistent with the pseudo-time–based differentiation inference, T_{ex}, EM-like, and *CX3CR1*$^+$ cells exhibited the most oligoclonal expansion based on scTCR-seq, suggesting antigen selection (*20*, *21*). However, among all cell states, P_{ex} and T_{ex} exhibited, in addition to exhaustion, the highest signatures of TCR signaling and cytotoxicity as well as proliferation (Fig. 3E), indicating tumor antigen engagement. Consistent with a precursor state, P_{ex} TILs overexpressed the most DNA amplification and repair pathways as well as proliferation signatures (Fig. 3E and fig. S4B). P_{ex} displayed higher TF activity of transcription factor 7 (TCF7), MYC, myogenic differentiation 1 (MYOD1), and histone deacetylase 2 (HDAC2) relative to T_{ex}, whereas T_{ex} exhibited higher Runt-related transcription factor 3 (RUNX3) regulon activity, a key regulator of $CD8^+$ T cell tissue residence, than P_{ex} (fig. S4C). Consistent with previous findings that a fraction of exhausted $CD8^+$ TILs retained the proliferative capacity as a consequence of CD28 costimulation received from dendritic cells (DCs) in situ (*22*), we found that T_{ex} and P_{ex} in baseline melanoma of Rs also exhibited signatures of CD28 costimulation and proliferation (Fig. 3E). Exhausted $CD8^+$ TILs with lower levels of CD28 costimulation exhibited lower eomesodermin (EOMES) and T-box transcription factor 21(TBX21) activities (fig. S4D), implying that a subset of T_{ex} cells might not have transitioned to terminal exhaustion, as also suggested by increased proliferation. TILs transition through a continuous gradient of exhaustion states (*21*), as suggested by our pseudo-time analysis (Fig. 3C and fig. S4A).

ISG $CD8^+$ TILs, distinguished by a dominant signature of IFN response genes, have been previously reported in human TILs (*20*). Here, ISG $CD8^+$ TILs exhibited oligoclonally expanded TCR sequences overlapping with exhausted $CD8^+$ TILs (fig. S4E) and displayed gene signatures of cytotoxicity, TCR signaling, and exhaustion, implying that ISG cells were antigen-experienced tumor-reactive T_{ex} located in IFN-rich tumor niches. A fraction of EM-like $CD8^+$ TILs exhibited the highest level of clonal TCR overlapping with the exhausted compartment, indicating that some of these cells were likely tumor-specific but not yet engaged in antigen recognition because they lacked signatures of TCR signaling or exhaustion (*20*). However, the frequencies of EM-like and *CX3CR1*$^+$ $CD8^+$ TILs were similar in Rs and NRs at baseline (Fig. 3D), likely reflecting that a proportion of these cells were derived from unrelated bystander cells. In agreement with the above findings, baseline $CD8^+$ TILs were enriched for transcriptomic programs of exhaustion, TCR signaling, cytotoxicity, CD28 costimulation, IL-2 signaling, IFN-γ activation, and effector function (Fig. 3F and fig. S4F). Using signatures denoting tumor neo-antigen reactivity (*9*, *10*), we validated that the tumor reactivity was higher in $CD8^+$ TILs of Rs. Conversely, $CD8^+$ TILs of NRs overexpressed a viral-specific signature, implying a bystander phenotype (Fig. 3F).

We analyzed differentially expressed genes in $CD8^+$ TILs from Rs and NRs deeper, at both single-cell and patient–pseudo-bulk levels. The correlation between logarithmic fold changes of these two levels [Pearson's correlation coefficient (r) = 0.80, $P < 10^{-216}$] revealed concordantly overexpressed genes (*CXCL13*, *CCL5*, *HLA-DRB5*, *HAVCR2*, *TNFRSF9*, *CTLA4*, and *PDCD1*) and regulons [RUNX3, EOMES, TBX21, nuclear factor of activated T-cells 5 (NFAT5), and ETS variant transcription factor 1 (ETV1)] in $CD8^+$ TILs of Rs (Fig. 3, G and H, and data file S2), many of which were previously associated with exhausted/CD28-costimulated $CD8^+$ TIL signatures (*22*). Moreover, clinical response was associated with baseline $CD8^+$ TILs that exhibited increased inferred activity of ZNF831 (zinc finger protein 831) and HIVEP1 (zinc finger protein 40). ZNF831 and HIVEP1 bind to enhancer elements of several key genes implicated in the effector and exhaustion programs, including the genes encoding the IL-2 receptor (*IL2RA*, *IL2RB*, and *IL2RG*) and *IFNB1*, *TBX21*/T-bet, *EOMES*, and *PRDM1*/BLIMP-1 implicated in transcriptional activation of multiple immune checkpoint genes, *ETV1*-targeting TOX, and *RUNX3* (Fig. 3H). Conversely, failure of TIL-ACT was associated with predominance of naive- and memory-like $CD8^+$ TILs at baseline, highlighted by the overexpression of *IL7R* and *LTB* as well as higher activity of TFs implicated in the WNT/β-catenin signaling pathway, including lymphoid enhancer factor 1 (LEF1) and TCF7, and the transforming growth factor (TGF)–β signaling pathway, including FOXP1 and SMAD3 (Fig. 3, G and H, and data file S2), reflecting the paucity of antigen-experienced tumor-reactive populations. Last, we computed a $CD8^+$ T cell signature score associated with the clinical response from (data file S2) Fig. 3G. $CD8^+$ T_{ex} and P_{ex}, followed by EM-like, were the TIL subsets that most highly overexpressed the T cell clinical response signature (Fig. 3I), confirming their relevance for TIL-ACT.

To identify potential differences in $CD8^+$ TILs between CRs and PRs, we conducted differential gene expression analysis. $CD8^+$ TILs from CRs overexpressed genes linked to improved T cell recruitment and infiltration (*CXCR3*, *CCL5*, and *CCL3*) (*23*) as well as higher TCR avidity (*CXCR3*) (*24*), tissue residence (*ITGAE*), and IL-2 signaling (*IL2RB* and *IL2RG*) (fig. S4G and data file S4). Pathway analysis revealed that besides higher IFN, TCR signaling, and CD28 costimulation, $CD8^+$ TILs of CRs displayed elevated pathways of mitochondrial potential and function, such as adenosine 5′-triphosphate and amino acid synthesis, electron transport chain, and cristae formation (fig. S4H and data file S4). These data imply that $CD8^+$ TILs of CRs have higher metabolic fitness that could enable them to withstand harsh TME conditions and mediate long-term clinical response.

We corroborated our transcriptomic findings of TILs by immunohistochemistry (IHC) and mIF microscopy interrogation on several formalin-fixed paraffin-embedded (FFPE) slides of baseline tumors. These analyses showed higher frequencies of intratumoral $CD3^+CD8^+$ TILs and $CD3^+CD8^+PD1^+$ TILs (located within tumor nests) in Rs (Fig. 3J and fig. S4, I and J). Patients with PD had the lowest densities of all $CD8^+$ TIL populations, validating the relevance of $CD8^+$ TIL for clinical response. In conclusion, in situ T cell

Downloaded from https://www.science.org at University of Lausanne on February 05, 2024

activation, cytotoxicity, costimulation, and exhaustion along with immunogenic tumor cells with higher TMB are hallmarks of melanoma response to TIL-ACT.

Other baseline lymphoid states in Rs and NRs

In examining other lymphoid cells at baseline, we found that T_{fh}-like $CD4^+$ *CXCL13*$^+$ cells and T_{reg} cells did not differ between Rs and pooled NRs, but progressors (PD) displayed the lowest proportions of T_{reg} cells (fig. S4K). We identified highly proliferative γδ T cells expressing *TRGC2* and *TRDV1*/*TRDC* TCR chains, killer cell lectin-like receptor (KLR) molecules (*KLR D1*/*K1*/*C2*/*C4*/*G1*), *CCL5*, *NKG7*, and granzymes (fig. S3E and fig. S4L) significantly enriched in NRs and specifically in patients with PD, suggesting a negative influence on TIL-ACT (fig. S4M).

The important role of tumor-resident B cells in supporting antitumor T cell responses and response to ICB is being increasingly recognized (*25*). In addition to plasma cells (*MZB1*$^+$), we identified follicular-like (*MS4A1*$^+$) tumor-resident $CD20^+$ B cells clustering in three main states: naive (*TCL1A*$^+$, *FCER2*$^+$, and *IGHD*$^+$), memory (*CD27*$^+$), and germinal center (GC) ($CD38^+$ and *MEF2B*$^+$) (fig. S5, A and B, and data file S5). Memory B cells displayed high levels of IFN signaling and mature antigen-presenting cell (APC) genes (*CD80*, *CD86*, and *CD40*), whereas GC B cells overexpressed signatures of B cell receptor (BCR) signaling, class II antigen presentation, and proliferation (fig. S5B). We could not detect significant differences in the proportions of B cells between Rs and NRs by scRNA-seq (fig. S5C) or by mIF analysis (fig. S5D). However, collectively, B cells from Rs, particularly memory cells, displayed increased IFN signaling and MHC class II antigen presentation, implying a possible participation in modulating local T cell immunity (fig. S5, A and B, and data file S5). In line with this observation, we saw that Rs had a trend for higher enrichment of tertiary lymphoid structures (fig. S5E).

TIL-ACT–responding melanomas are infiltrated by activated macrophages and DCs

A mounting body of evidence indicates that the organization of the tumor myeloid compartment is crucial for orchestrating T cell immunity. For example, tumor-resident myeloid cells promote intratumoral T cell engraftment (*23*) and support $CD8^+$ T_{ex} effector functions via CD28 costimulation (*22*), and macrophage states predict response to checkpoint immunotherapy in melanoma, breast, and renal cancer (*26*). On the basis of scRNA-seq data obtained from all patients, we detected 11 clusters of myeloid cells, which we annotated according to well-described datasets (*27*, *28*) into four DC states [DC1, DC2, *CCR7*$^+$ DC3, and plasmacytoid (pDCs)], five macrophage states (*CXCL9*$^+$, ISG, *S100A8*$^+$, *TREM2*$^+$, and *C1Q*$^+$ macrophages) and two monocyte states [monocytes and monocyte-like DCs (monoDC)]. Each of these states was also characterized by distinct inferred regulon activities (Fig. 4A; fig. S5, F and G; and data file S5).

When comparing myeloid cells from Rs and NRs, the relative proportions of DCs and monocytes/macrophages were similar both by scRNA-seq (fig. S5H) and by mIF analysis (fig. S5I). We also observed no statistically significant differences when analyzing each of the 11 individual myeloid cell states except for monoDCs that were more abundant in NRs (fig. S5H). Considering that macrophage polarization may have either anti- or protumor effects (*26*), we investigated whether such polarization differed between Rs and NRs. Because macrophages can express M1- and M2-like phenotypes (fig. S5G) that have been associated with the ability to promote or suppress T cells, respectively, at least in vitro, we asked whether the ratio of macrophages with canonical M1 and M2 markers in baseline tumors was associated with clinical response. We assigned each macrophage to an M1 and/or M2 phenotype using M1 and M2 gene signatures and quantified their ratios. We found that Rs had a higher, albeit not statistically significant, M1/M2 ratio compared with NRs (fig. S5J).

We further analyzed differentially expressed genes in macrophages between Rs and NRs, at both single-cell and patient–pseudobulk levels. This analysis unveiled robustly overexpressed genes involved in IFN signaling (*IFI27*, *IFITM1*, *IFITM3*, *IFI6*, and *STAT1*), complement component synthesis (*C1QA-C* and *C3*), phagocytosis, and antigen processing and presentation (*HLA-B*, *HLA-C*, *B2M*, *HLA-DQA1*, *HLA-DQA2*, and *HLA-DRB5*), as well as up-regulation of IFN-inducible chemokines *CXCL9* and *CXCL10* in macrophages of Rs (Fig. 4, B and C, and data files S2 and S4). We next computed a clinical response-associated macrophage score using the most up-regulated genes in Rs (Fig. 4D and data file S2) and interrogated various macrophage subsets. Revealing their relevance for TIL-ACT, this signature was highly overexpressed in *CXCL9*$^+$ and ISG macrophages followed by *C1Q*$^+$ and *TREM2*$^+$ cells, specifically in Rs (Fig. 4E and fig. S5K). CXCL9 in macrophages is specifically up-regulated by IFN-γ (*23*), indicating the presence of nearby TILs recognizing tumor antigen, whereas it further amplifies intratumoral TIL engraftment (*23*). Because both *CXCL9*$^+$ and ISG macrophages overexpress *CXCL9*, they are likely engaged in important cross-talks with tumor-specific T cells in situ at baseline. As expected, *S100A8*$^+$ macrophages, which have been associated with tumor promotion and express immunosuppressive programs (fig. S5, F and G), did not contribute to the gene signature associated with clinical response (Fig. 4, D and E).

Next, we conducted similar analyses for DCs. As for macrophages, DCs exhibited increased activation and IFN response signatures (*IRF4-7*, *CXCR4*, *ICAM1*, and *STAT1*) in Rs (Fig. 4, F and G; fig. S5, F and G; and data file S2), revealing an overall type 1 polarization of the myeloid compartment. We next derived an integrated DC-specific clinical response signature as above. This signature was largely confined to pDCs in Rs (Fig. 4, H and I). Although the role of pDCs in cancer is not clear presently, the presence of pDCs in human colon cancer has recently been associated with increased PFS and OS (*29*).

Last, we examined the relative abundance of tumor-reactive $CD8^+$ TILs over myeloid subsets, focusing on exhausted TILs (T_{ex} and P_{ex} combined). The frequency of exhausted TILs relative to macrophages or DCs was significantly higher in Rs (Fig. 4J). In conclusion, specific transcriptional programs, such as complement activation, IFN signaling, IFN-inducible chemokines, antigen presentation, and CD28 costimulation, dominate the phenotype of macrophages and DCs in baseline tumors responding to TIL-ACT.

Melanomas responding to TIL-ACT are characterized by a rich immune cell cross-talk

The above findings raised the possibility that important cellular cross-talks established between TILs and tumor APCs at baseline provided the bases for successful TIL-ACT. We therefore inferred cell-to-cell cross-talks through ligandome analysis by computing receptor-ligand gene expression and relative proportions of putative

Downloaded from https://www.science.org at University of Lausanne on February 05, 2024

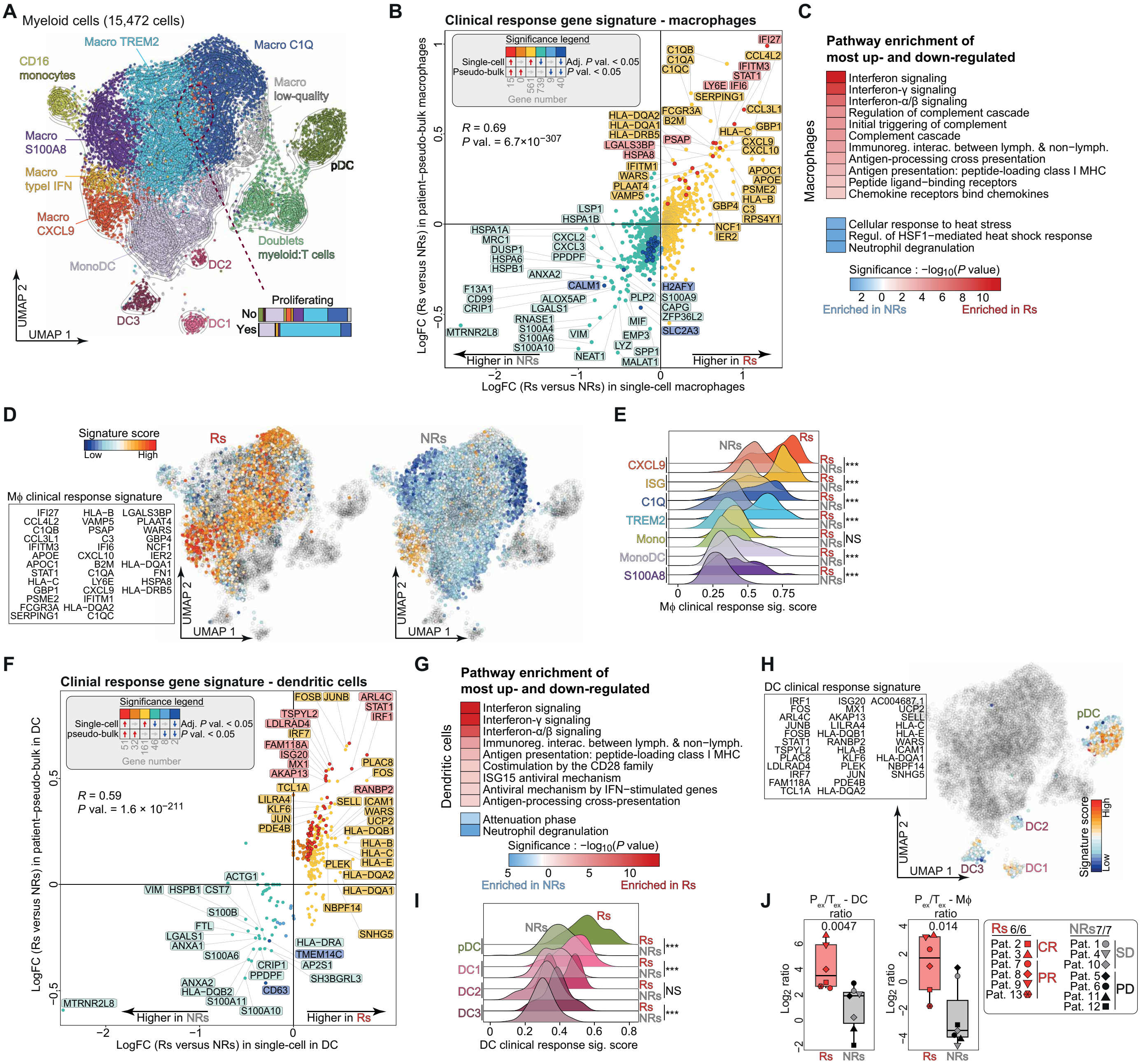

Fig. 4. Activation of the myeloid compartment is associated with response to TIL-ACT. (**A**) UMAP projection showing subclustering of myeloid cells from CD45$^+$ cell–sorted data from 13 baseline and seven post-ACT tumors. (**B**) Differential gene expression analysis between macrophages from Rs versus NRs in baseline tumors at single-cell (*x* axis) and patient–pseudo-bulk (*y* axis) levels. (**C**) Most up-regulated and down-regulated genes in macrophages between Rs and NRs (from B) were subjected to reactome enrichment analysis, and selected significant (FDR-adjusted $P < 0.01$) pathways are shown. (**D**) Macrophage clinical response gene signature (left) and its scoring projected in UMAP space in baseline tumors (split for Rs and NRs). (**E**) Ridge plot displaying the macrophage clinical response signature score per macrophage subsets split according to response in baseline tumors. (**F**) Differential gene expression analysis between DCs from Rs versus NRs in baseline tumors at single-cell (*x* axis) and patient–pseudo-bulk (*y* axis) levels. (**G**) Most up-regulated and down-regulated genes in DCs between Rs and NRs (from F) were subjected to reactome enrichment analysis and selected significant (FDR-adjusted $P < 0.01$) pathways are shown. (**H**) DC clinical response gene signature [from (F)] and its scoring projected in UMAP space in baseline tumors. (**I**) Ridge plot displaying the DC clinical response signature score per DC subsets split according to clinical response in baseline tumors. (**J**) Log$_2$ ratio of the proportions (out of CD45$^+$ cells) between exhausted T cells (union of CD8 P_{ex} and T_{ex}) and bulked DC or macrophage populations in single-cell data of baseline tumors. Statistical significance was assessed using linear regression (B and F), Wilcoxon rank sum test (J), and by Bonferroni-adjusted one-sided Student's *t* test (E and I). Triple asterisks (***) in (E) and (I) denote adjusted $P < 0.001$. NS, not significant.

Downloaded from https://www.science.org at University of Lausanne on February 05, 2024

cell pairs in the TME. These analyses revealed far more significant immune cell-to-cell interactions in tumors of Rs relative to NRs at baseline (Fig. 5A), because there was a plethora of putative interactions implicating $CD8^+$ and $CD4^+$ TIL subsets with myeloid subsets in Rs (fig. S6A and data file S6). The only significant interactions identified in NRs were mostly occurring between tumor cells and other cell types like *S100A8*$^+$ macrophage subsets that expressed uniquely M2- but not M1-like signatures (fig. S5G), endothelial cells, and DC2s, but TILs appeared not involved (fig. S6A).

To increase resolution in the interactome, we focused our analysis on five pathways that emerged in the analyses of the T, B, and myeloid compartments and were critical for clinical response to immunotherapy (*30*): complement, IFN, chemokines, ILs, and costimulation/coinhibition (data file S7). Again, we inferred a higher number of putative significant interactions between TILs and myeloid cells, TILs and tumor cells, and $CD4^+$ and $CD8^+$ TILs in Rs (Fig. 5B, and fig. S6B) and found cross-talk between TIL subsets predicted to be tumor-specific, including exhausted, ISG, and EM-like cells, with several macrophage subsets and DCs (Fig. 5C). Terminally exhausted and ISG T cells were predicted to interact predominantly with *C1Q*$^+$ and *CXCL9*$^+$ macrophages, whereas P_{ex} and EM-like T cells were predicted to interact with *TREM2*$^+$ and *S100A8*$^+$ macrophages. On the basis of available molecules, *CXCL9*$^+$ macrophages could attract exhausted $CD8^+$ TILs expressing *CCR5*, *CXCR3*, or *CXCR5* through *CCL5*, *CXCL9/10/11*, or *CXCL13* and could establish adhesive interactions with them through *ICAM1* and *ICAM2* expressed on macrophages and *ITGB2* and *ITGAL* expressed on TILs (Fig. 5D). Through such interactions, *CXCL9*$^+$ macrophages could establish important niches, as seen in ovarian cancer (*22*), to support T_{ex} function through CD28 and other costimulatory ligands. Further chemotactic and stimulatory interactions could be mediated locally by complement components, because *C3* was up-regulated in exhausted TILs, whereas *C3AR1* was expressed by complement-positive and *CXCL9*$^+$ macrophages (Fig. 5D). T cells up-regulate and release C3 upon TCR engagement and CD28 costimulation, which can drive APC maturation and further T cell costimulation (*31*, *32*). *C1Q*$^+$ macrophages expressed IL-15, which would provide key survival and stemness-promoting signals to local TILs in such putative niches through *IL15RA-IL2RG* (Fig. 5D and data file S8) (*33*).

We sought to validate these hypotheses by specifically examining physical cell doublets identified during single-cell analyses. We detected doublets occurring between T and myeloid cells (Fig. 4A, B) and T cells (fig. S5A), as well as $CD4^+$ and $CD8^+$ T cells characterized by higher number of expressed genes per cell and carrying gene expression profiles from both of their respective counterparts (fig. S6C). It is widely accepted that doublets can arise technically after tissue dissociation when two or more cells are encapsulated in the same droplet. To test whether they could be composed by true physical pairs of cells, as reported by others (*34*), we visualized T-myeloid doublets in baseline tumors upon tissue dissociation by flow cytometry imaging analysis (ImageStream). We observed the presence of interacting cell doublets that coexpressed surface CD3 and CD14 and mediated synapses in melanoma tumor dissociates (0.05%) (fig. S6D). This indicates that, although we cannot completely avoid the bias of artifactual doublets being present in our tumors after dissociation, real physical doublets were captured.

In line with the above inferred cross-talks (Fig. 5, B to D), we found a higher frequency of T-myeloid cell doublets and trends of higher frequencies of T-B and $CD4^+$-$CD8^+$ T cell doublets in Rs (Fig. 5E and fig. S6E). We detected overexpression of T cell exhaustion along with CD28 costimulation signatures in T cell–myeloid doublets from Rs, implying that exhausted $CD8^+$ TILs engaged in these doublets received CD28 costimulation from the cognate myeloid cells (Fig. 5F). Similarly, B–T cell doublets exhibited higher expression of T cell costimulatory and tumor-reactivity signatures, implying that B cells could also provide CD28 costimulation to their paired tumor-specific $CD8^+$ TILs (fig. S6F). Last, $CD4^+$-$CD8^+$ T cell doublets overexpressed scores of cytotoxicity and tumor reactivity, implying important cross-talks between tumor-specific $CD8^+$ TILs and cognate $CD4^+$ helper cells (fig. S6F). By deconvoluting cell states involved in cell doublets, we found that T-myeloid doublets were enriched specifically in *CXCL9*$^+$ macrophages and $CD8^+$ P_{ex} or T_{ex} cells (Fig. 5G and fig. S6G). Thus, these key cell cross-talks were prevalent between tumor-reactive $CD8^+$ TILs and properly polarized macrophages and were likely critical to the recruitment and functional support of these tumor-specific $CD8^+$ T cells, explaining their strong association with response to TIL-ACT. Conversely, T-myeloid doublets were rare in NRs and were mostly enriched in NK-like $CD8^+$ T cells and DC2 (Fig. 5G and fig. S6G).

Furthermore, we used mIF to identify $CD8^+PD\text{-}1^+$ or $CD8^-PD\text{-}1^+$ TILs, $CD11c^+$ or $CD68^+$ myeloid cells, and $CD19^+$ B cells and examined their mutual interactions in situ (Fig. 5, H to J). We found higher densities of $CD11c^+$ cells (fig. S6H) and detected higher numbers of mutual interactions between $CD8^+$ or $CD8^+PD\text{-}1^+$ TILs and $CD11c^+$ cells in both tumor islets and the stroma compartment in Rs compared with those in NRs using neighborhood analysis examined at different radii (20, 45, and 100 μm) (Fig. 5, J to L, and fig. S6, I and J). Although cell frequencies and their mutual interaction are interdependent by design, we found that the mutual interaction between $CD8^+$ and $CD11c^+$ cells was separating more signficantly Rs and NRs than their respective minimal cell frequency (Fig 5L and fig. S6K). Furthermore, $CD8^+PD\text{-}1^+$:$CD68^+$, $CD8^+PD\text{-}1^+$:$CD19^+$, or $CD8^+PD\text{-}1^+$:$CD8^-PD\text{-}1^+$ (i.e., $CD4^+PD\text{-}1^+$ T cells) pairs were also higher in the stroma of Rs (Fig. 5J and fig. S6I). These analyses collectively revealed dense immune cell networks in the TME of Rs at baseline, unlike in NRs.

We sought to understand deeper, at the protein level, the states of TILs and myeloid cells residing within T cell-myeloid neighborhoods. We applied the GeoMx protein panel selectively on regions of interest (ROIs) enriched with T cell–myeloid niches (Fig. 5M and data file S9). Differential protein expression comparing 74 targets between baseline melanomas of Rs and NRs revealed that T cell–myeloid niches of Rs were enriched with proteins, suggesting higher antigen expression (NY-ESO-1) and presentation (B2M) and potentially higher tumor-cell killing [cleaved caspase-9, BCL2, and poly(adenosine 5′-diphosphate–ribose) polymerase] (Fig. 5N and data file S9). In addition, these niches were enriched with costimulating myeloid cell states (CD45, CD11c, PDL1, HLA-DR, and CD40) and activated, tumor-reactive, antigen-experienced, costimulated, and memory $CD8^+$ TILs denoted by overexpressions of CD8, CD127, GZMA, CD45RO, and CD25 (IL-2RA). TILs in these niches also overexpressed TIM3, cytotoxic T-lymphocyte associated protein 4 (CTLA-4), and tumor necrosis factor receptor superfamily member 9 (4-1BB), validating them as leading biomarkers of our $CD8^+$ TIL ACT clinical response signature (Fig. 3G). In contrast, T cell–myeloid niches of NRs were characterized by overexpressions of p53, glyceraldehyde-3-phosphate dehydrogenase (GAPDH), Ki67,

Downloaded from https://www.science.org at University of Lausanne on February 05, 2024

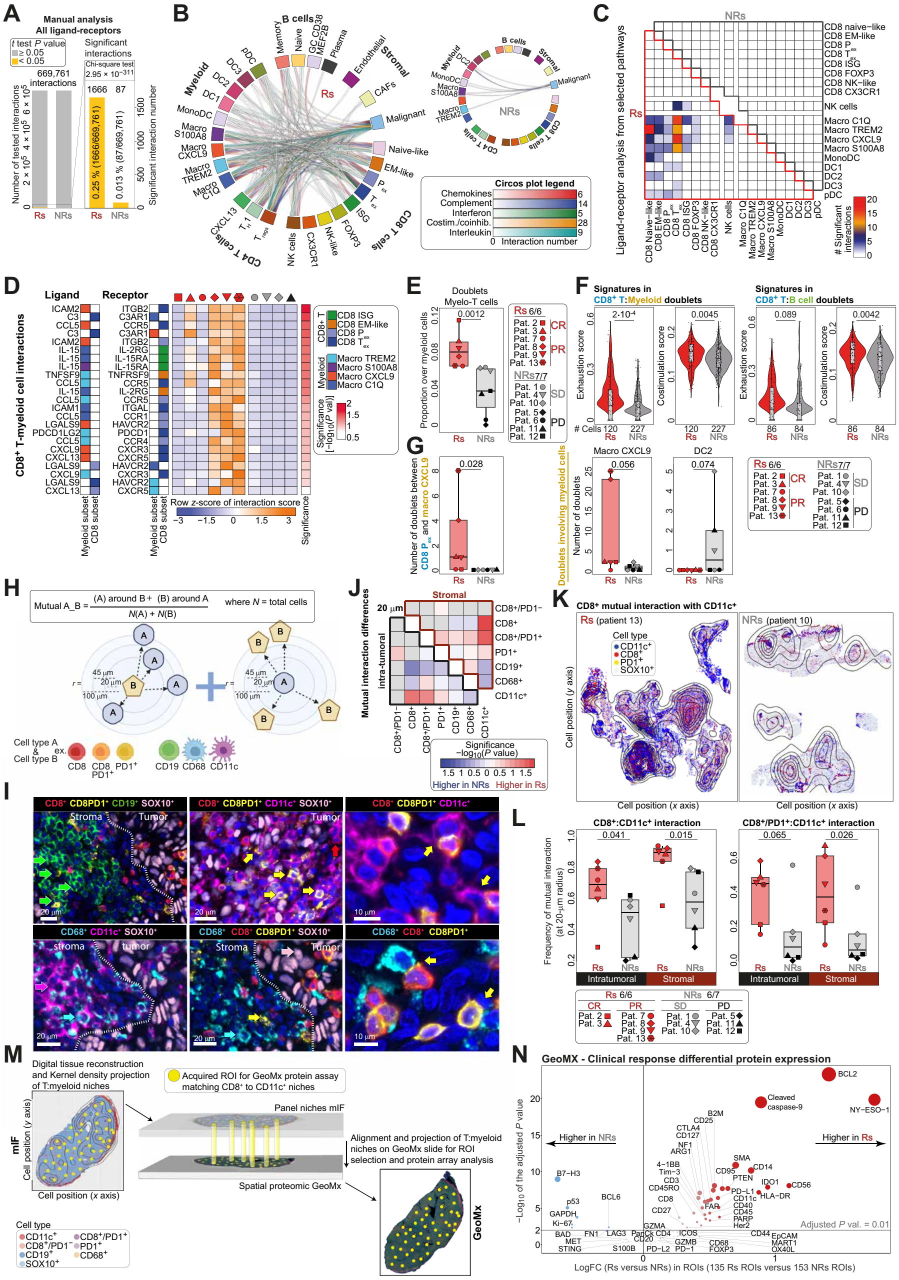

Fig. 5. Baseline tumors of TIL-ACT Rs are characterized by a rich T cell–TME cross-talk. (**A**) The left bar plot shows the total number of tested and significant (unadjusted Student's *t* test $P < 0.05$) interactions detected between Rs and NRs. The right bar plot (right) shows enlarged view that better captures significant interactions. Statistical analysis to assess whether the number of significant interactions was different between Rs and NRs was performed using chi-square test taking into account the total possible number of interactions. (**B**) Circos plots showing cell subtypes involved in significant interactions (link) and the number of significant interactions (in color intensity) for the ligand-receptor pairs of five different pathways and split by clinical response in baseline tumors. (**C**) Heatmap displaying the number of ligand-receptor [from selected pathways like in (B) to (D)] interactions between cell subsets found significantly higher in responders (bottom-left part of the heatmap) or nonresponders (top-right part of the heatmap). (**D**) Heatmap displaying interaction scores for each patient and for selected ligand-receptor interactions between myeloid and CD8$^+$ T cell subtypes in baseline tumors. (**E**) Box plots showing the proportion of T-myeloid cell doublets. (**F**) Selected signature scores computed in doublets involving CD8$^+$ T cells and myeloid cells (left) or CD8$^+$ T cells and B cells (right). (**G**) Examples of specific cell subsets involved in the doublet deconvolution according to clinical response. (**H**) Scheme and formula depicting how the distance between two different cell types in cell mutual interaction analysis was computed. (**I**) Example images of mIF staining for the indicated markers in tumors. (**J**) Heatmap showing the differences in the frequency of mutual interaction between cell types at a 20-μm neighboring radius. (**K**) Representative images of digital tissue reconstruction showing the density of the frequency of mutual interaction between CD8$^+$ and CD11c$^+$ cells according to clinical response. (**L**) Box plots displaying frequency of mutual interaction between the indicated cell types according to clinical response and split by stromal or intratumoral areas. (**M**) Scheme depicting the ROI selection strategy for spatial GeoMx profiling. (**N**) Volcano plot displaying differential protein expression analysis performed by comparing ROIs from six Rs ($n = 135$) versus six NRs ($n = 153$) profiled by spatial GeoMx. Statistical significances were assessed using Wilcoxon rank sum test (E, G, J, and L), two-sided Student's *t* test (A to D and F), and linear regression (N).

Downloaded from https://www.science.org at University of Lausanne on February 05, 2024

and MET, indicating mostly tumor cell proliferation, and B7-H3 (Fig. 5N and data file S9). Overall, intratumoral T cell–myeloid niches and other T cell networks likely recruit and nurture tumor-reactive TILs and are the basis of generating effective responses to TIL-ACT therapy.

Effective TIL-ACT therapy reprograms myeloid populations and reconstitutes antitumor CD8$^+$ TIL–myeloid cell networks

Next, we sought to determine how TIL-ACT affected TME dynamics by using bulk RNA-seq data from tumors at baseline (T0) and biopsies acquired a minimum of 30 days after ACT (T30) (fig. S1A) to capture changes in the TME of Rs versus NRs. Oncogenic epidermal growth factor receptor, erb-b2 receptor tyrosine kinase 2 (ERBB2)/protein tyrosine kinase 6, and PI3K/ERBB4 signaling–related pathways in T30 biopsies were either down-regulated solely in Rs or up-regulated uniquely in NRs, possibly reflecting tumor cell expansion or adaptation (Fig. 6A, fig. S7A, and data file S10). Responding tumors exhibited an increase in numerous inflammatory signatures (alternative complement activation, scavenger receptors, Toll-like receptor 3, NF-κB, IL-18, and IL-10 signaling), denoting reinvigoration of innate immunity after ACT. T cell activation [CTLA-4, programmed cell death 1 (PD-1), TCR, CD28, IL-2, and FasL signaling] and B cell activation (BCR signaling) were specifically lost in NRs after ACT biopsies. These pathways were already lower at baseline in tumors of NRs relative to Rs (see also fig. S4F) and were lost in NR T30 biopsies (Fig. 6A).

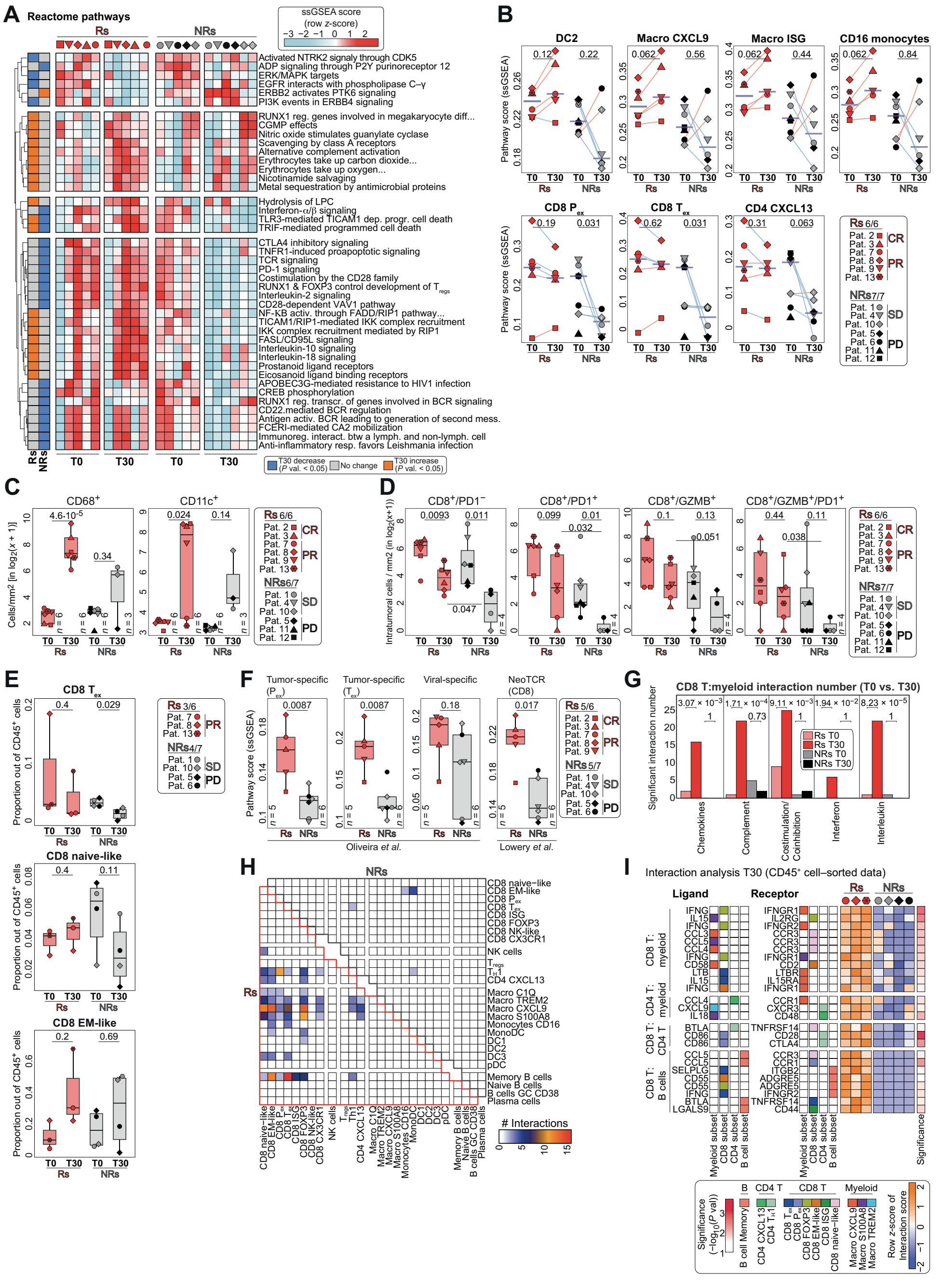

Fig. 6. Dynamics of TME and TIL-TME interactions associated with clinical response before and after TIL-ACT. (**A**) Heatmap displaying reactome pathway scores that were significantly different between T0 and T30 either in Rs or in NRs. FADD, Fas-associated death domain protein. NTRK2, neurotrophic tyrosine kinase receptor type 2. LPC, lysophosphatidylcholine acyltransferase. TRIF, toll/IL-1 receptor domain-containing adapter-inducing IFN-β. TICAM, toll-like receptor adaptor molecule. RIP1, receptor-interacting serine/threonine-protein kinase 1. IKK, IκB kinase. APOBEC3G, apolipoprotein B mRNA editing enzyme, catalytic polypeptide-like 3G. (**B**) Line plots showing signature scores in the bulk RNA-seq, using gene signatures specific to cell types captured in our scRNA-seq data, split by clinical response and ACT time. (**C**) Box plots of cell densities profiled by mIF and split by clinical response and ACT time for CD68 and CD11c stainings. (**D**) Box plots of intratumoral cell densities profiled by mIF split by clinical response and ACT time for the indicated stainings. (**E**) Box plots showing the dynamics of CD8 T_{ex}, CD8 naive-like, and CD8 EM-like proportions (out of $CD45^+$ cells in single-cell data) from T0 to T30. (**F**) Box plots showing signature scores in the bulk RNA-seq data split by clinical response in T30. (**G**) Number of significant (unadjusted Student's *t* test $P < 0.05$) ligand-receptor pair interactions between $CD8^+$ T and myeloid cells categorized into five different pathways and split by clinical response and ACT time. Data were extracted from exhaustive fig. S7C. Statistical analyses to assess whether the number of significant interactions was different between T0 and T30 were performed using chi-square test taking into account the total possible number of interactions at T0 and T30. (**H**) Heatmap displaying the number of ligand-receptor (from the five selected pathways like in Fig. 5C) interactions between cell subsets found significantly higher in responders (bottom-left part) or nonresponders (top-right part) in T30. (**I**) Heatmap displaying interaction scores for each patient and for selected ligand-receptor and cell-type interactions in T30 tumors. Statistical significances were assessed using linear regression (A), paired Wilcoxon rank sum test (B), Wilcoxon rank sum test (E and F), and two-sided Student's *t* test (C, D, and G to I).

To infer evolution dynamics in specific immune cell subets, we interrogated bulk RNA-seq data at baseline and after ACT by using gene signatures that discriminate for cell subtypes, which we derived from our scRNA-seq data. We observed a reconstitution after ACT of key TME hallmarks observed at baseline, including maintenance of $CD8^+$ P_{ex} and T_{ex} and *CXCL13*$^+$ $CD4^+$ TIL signatures, but only in Rs. Conversely, NRs lost signatures of $CD8^+$ P_{ex} and T_{ex}, *CXCL13*$^+$ $CD4^+$ TILs, T_{reg} cells, and DC2 (Fig. 6B). TIL-ACT increased signatures for *CXCL9*$^+$, ISG macrophages, and $CD16^+$ monocytes in Rs specifically (Fig. 6B). This observation was also validated by mIF analysis, which showed increased densities of both infiltrating $CD68^+$ and $CD11c^+$ myeloid cells from baseline to after ACT (Fig. 6C). Moreover, by mIF, we confirmed that Rs maintained a relatively elevated frequency of $CD8^+$ TILs expressing PD-1 and/or granzyme-B after ACT, whereas NRs displayed significantly lower frequencies of such tumor-reactive $CD8^+$ TILs after ACT relative to their baseline (Fig. 6D). We observed a decrease in the frequency of intratumoral $CD8^+PD\text{-}1^-$ TILs in both Rs and NRs, likely representing bystander T cells not engaging tumor cells that were lost because of host lymphodepletion. We validated the above finding at the single-cell level in 7 of the 13 patients. We found that NRs, but not Rs, lost their CD8 T_{ex} infiltration after ACT (Fig. 6E and fig. S7B).

Downloaded from https://www.science.org at University of Lausanne on February 05, 2024

Applying tumor neo-antigen reactivity T cell signatures (*9*, *10*) in T30 bulk RNA-seq, we found that Rs' CD8$^+$ TILs persisting after ACT exhibited higher tumor-specific signatures (Fig. 6F).

We next asked whether the previously described cellular cross-talks could also be reconstituted in the TME after TIL-ACT. Analysis of the available paired scRNA-seq data from baseline and after ACT in seven patients revealed that many of the original cross-talks were potentially reestablished, with a marked increase in predicted putative interactions specifically between the CD8$^+$ and the myeloid compartment at T30 compared with that at baseline, specifically in Rs (Fig. 6, G and H, and fig. S7C). We also performed paired neighborhood analysis in melanomas from 9 of the 13 patients. In line with the interactome predicted from the scRNA-seq data, we observed increased CD8$^+$ T cell:CD68$^+$ macrophage niches in both CRs and two of the four PRs, whereas these were reduced in the PD and one of the two SDs (fig. S7D).

From paired scRNA-seq data of baseline and post-ACT tumors, we identified again the main CD8$^+$ TIL states related to tumor immune recognition, as recognized at the steady state, i.e., P_{ex}, T_{ex}, EM-like, and ISG cells. Most of them were predicted to interact densely with the key myeloid subsets, especially *CXCL9*$^+$ macrophages (Fig. 6H and fig. S7E). Although most of the tumor-resident B cells were depleted after ACT, EM-like, T_{ex}, and ISG CD8$^+$ TILs were also predicted to interact with the available memory B cells (Fig. 6H and fig. S7E). The interactions between *IFNG* and *IFNGR1/2* on CD8$^+$ TIL and macrophages, respectively, implied a direct macrophage polarization by TILs, leading to upregulation of *CXCL9* and *CXCL10*. The production of additional chemokines by these activated macrophages, such as *CCL3*, *CCL4*, and *CCL5*, explained partly how rich chemokine circuitries could help reestablish the diverse inflammatory infiltrate in these tumors after ACT (Fig. 6I and data file S11). Conversely, as in baseline tumors, we could not predict any meaningful immune cell interactions in NRs, which were mainly predicted between CD16$^+$ monocytes or monoDCs with EM-like CD8$^+$ TILs (Fig. 6H and fig. S7E). These results suggested that successful ACT not only restored the TIL repertoire but also reprogrammed the tumor macrophage population toward *CXCL9*$^+$ cells, thereby strengthening the potential CD8$^+$ T-myeloid interactome.

Thus, successful TIL-ACT leads to the elimination of melanoma through the establishment of a favorable TME, with re-engraftment of tumor-reactive TILs after ACT and improvement of the myeloid compartment after immune reconstitution. The close association of exhausted CD8$^+$ TILs with CD11c$^+$ myeloid cells represents a potential biomarker for patient selection for TIL-ACT therapy.

DISCUSSION

This study presents a comprehensive single-cell profiling of longitudinal melanoma samples from patients who received TIL-ACT, providing insights into the TME and the cellular networks associated with clinical response to TIL-ACT. Our comparative analysis reveals that benefit from TIL-ACT is associated with preexisting immunity in the TME and is characterized by higher immunogenic tumor cells and tumor-reactive CD8$^+$ TILs (*9*, *10*, *22*, *35*). We found that tumor-reactive CD8$^+$ TILs were engaged in complex and meaningful cell networks. Myleoid cells were among the key cellular populations contributing to these interactions and bore distinct signatures in Rs, specifically overexpressing antigen-processing and presentation, costimulatory and type I IFN signatures, and CXCL9/10 chemokines. Recent studies have demonstrated the relevance of tumor-intrinsic (*36*) and myeloid-mediated DNA-sensing stimulator of interferon genes (STING) activation for the tumor IFN signaling (*37*), the recruitment of TILs, and the orchestration of antitumor immune response (*38*). These rely on the cooperation of CCL5 and CXCL9/10 chemokines, which ensure recruitment and retention of TILs in the TME by intratumoral myeloid cells (*23*) and promote response to ICB (*39*). Furthermore, CXCL9/10-expressing myeloid cells are associated with the presence of CXCL13-expressing TILs (*40*). These chemotactic interactions, along with the appropriate adhesion partners reported here, provide the basis for the formation of cell pairs between effector TILs and myeloid cell partners.

In baseline melanoma responsive to TIL-ACT therapy, we predicted the cellular interactome by ligandome analysis and documented a strong intratumoral cross-talk in chemokine, complement, and IFN pathways and adhesions between tumor-reactive CD8$^+$ TIL and activated myeloid cells. Although traditionally considered undesirable in scRNA-seq analyses, doublets can provide valuable information on immune cell interactions (*34*). We validated these interactions by demonstrating physical TIL-myeloid cell doublets and by quantifying cellular neighborhoods in situ through mIF and niche analysis in the tumor of origin, which revealed denser clusters of intratumoral T cell–myeloid niches in Rs at baseline. On the basis of scRNA-seq findings, the T cell–myeloid doublets were largely populated by CD8 T_{ex} and IFN-activated myeloid cells, supporting the specific implication of these cell subsets in driving T cell response at baseline. In addition to recruiting TILs, IFN-activated myeloid cells can also endow them with costimulatory signals (*22*), thereby providing a rich repertoire of relevant polyfunctional TILs at baseline that can be subsequently expanded ex vivo for TIL-ACT. The TME of NRs displayed minimal numbers of those interactions and almost no cellular cross-talk when focusing on pathways such as costimulation, complement, type I IFN, and chemokines.

Many of the above cellular cross-talks may be also implicated in driving responses to ICB. However, our Rs did not respond to prior mono- or dual-ICB, indicating that additional inhibitory mediators are active in the TME at baseline, preventing response to ICB, but that could have been eliminated upon TIL-ACT. TIL reinvigoration by ex vivo expansion and host lymphodepletion could contribute to overcoming TME suppression. When comparing the dynamics of TIL and TME states from baseline to after ACT, we observed that tumor-reactive TILs are preponderant, the frequency of IFN-activated myeloid cells increased, and the T cell–myeloid interactome further increased and diversified. This indicated that effective TIL-ACT reprograms myeloid populations and increases antitumor CD8$^+$ TIL-myeloid cell networks. Such interactive immune TMEs could sustain the persistence and functionality of ex vivo reinvigorated and adoptively transferred T cells via additional costimulatory signals.

Our detailed characterizations of TME states and dynamics as well as cell-cell interactome will help facilitate the development of biomarkers for ACT response and guide the next generation of adoptive cell–based immunotherapies to achieve maximal clinical benefit. Our findings suggest that tissue signatures documenting the presence of intratumoral tumor–reactive TIL-myeloid niches with traits of polyfunctionality, fitness, and costimulation can be used to select patients who likely would maximally benefit from TIL-ACT approaches with traditional IL-2–based TIL expansion methodologies.

Downloaded from https://www.science.org at University of Lausanne on February 05, 2024

Note that the small sample size of our trial cohort and the heterogeneity of prior lines of therapy received by these patients may limit final conclusions. Larger trials are required to further validate and extend these findings in melanoma and other cancer types. Although a recent trial has demonstrated higher PFS of TIL-ACT versus anti-CTLA4 therapy (*4*), how TIL-ACT will perform after dual anti-CTLA4 and anti–PD-1 combination remains an open question warranting investigation.

MATERIALS AND METHODS

Study design

We interrogated tumor-microenvironment cellular states and interactions of longitudinal samples from 13 patients with metastatic melanoma treated with TIL-ACT in our phase 1 clinical study (NCT03475134) using scRNA-seq and bulk RNA-seq, mIF, and spatial proteomic analyses in pre- and post-ACT tumor tissues. The number of data points used for analyses is indicated within the figures or in the figure legends.

Clinical trial design

From March 2018 to December 2020, we enrolled 15 patients in a single-center phase 1 investigator-initiated trial designed to test the feasibility of TIL-ACT in our center (ClinicalTrials.gov, NCT03475134). Among them, two patients did not receive any trial treatment: one patient failed during the rapid expansion phase (REP)–TIL and another one withdrew informed consent from the study before the start of the treatment. Thirteen eligible patients constitute the "per-protocol" cohort of the study for efficacy analysis (data file S1). Eligible patients were adults with histologically proven unresectable locally advanced (stage IIIc) or metastatic (stage IV) melanoma (12 cutaneous melanoma and one mucosal melanoma) who have progressed on at least one standard first line therapy, including but not limited to chemotherapy; BRAF and mitogen-activated protein kinase (MAPK) inhibitors; anti-CTLA4, anti–PD-1 or anti-LAG3 antibodies; and/or the combination. When feasible, a biopsy of one metastatic deposit was performed at screening to assess and quantify the intratumoral $CD3^+$ and $CD8^+$ T cell infiltration by a dedicated pathologist (J.D.). In some cases, archived FFPE material from diagnosis was retrieved for analysis. Patients were required to have an accessible metastatic site to procure for TILs with acceptable anticipated perioperative risk and also at least one separate additional measurable tumor lesion on CT to be followed according to RECIST 1.1 criteria. Inclusion criteria included good general health status [eastern cooperative oncology group performance status (ECOG PS) ≤ 2], sufficient cardiopulmonary function, including a cardiac stress test showing no reversible ischemia, adequate respiratory function with forced expiratory volume in 1 s (FEV1) $\geq 65\%$ predicted, forced vital capacity $\geq 65\%$ predicted and diffusing capacity of the lungs for carbon monoxide (DLCO) $\geq 50\%$ predicted corrected, and left ventricular ejection fraction $> 45\%$. Patients with active autoimmune conditions or acquired immunodeficiency were excluded. Patients were required to have adequate normal organ and marrow function, defined as hemoglobin ≥ 8 g/100 ml; absolute neutrophil count $\geq 1.0 \times 10^9$ ($\geq$1000 mm^{-3}); platelet count $\geq 100 \times 10^9$ (>100,000 mm^{-3}); serum creatinine $\leq 1.5\times$ of the institutional upper limit of normal; and aspartate aminotransferase and alanine aminotransferase $\leq 3\times$ of the institutional upper limit of normal. Patients with symptomatic and/or untreated brain metastases were excluded. Patients with definitively treated brain metastases were considered for enrollment as long as lesions were stable for $\geq$14 days before the beginning of the non-myeloablative (NMA) chemotherapy, with no evidence of previously unidentified lesions and no requirement for corticosteroid treatment. Bridging therapy was allowed as per investigator choice and upon discussion with the principal investigator.

Clinically eligible patients underwent surgery for TIL harvest and ex vivo expansion. Only patients having sufficient numbers of pre–REP-TILs (TIL number higher than 50 millions) were offered to receive TIL-ACT treatment. TILs were successfully expanded for all 13 patients from tumor deposits resected by surgery, and the median number of TILs infused was 55.0 billion cells (range, 12.8 to 84.7).

The primary endpoints were feasibility and safety of ACT using autologous TILs in our center. Key secondary endpoints were assessment of clinical efficacy of the treatment with respect to objective response rate (ORR) and PFS, according to RECIST1.1 and tumor response by iRECIST, as well as OS for a maximum of 5 years. In particular, ORR was defined as the best overall response (CR or PR) across all assessment time points, according to RECIST v. 1.1 and iRECIST criteria. Detailed measurements at different time points (1, 3, and 6 months) are reported in data file S1. The median follow-up time was of 45.4 months with an IQR ranging from 40.9 to 50.3. OS was defined as the time from start of NMA chemotherapy until death from any cause. If there was no death date, then the patient was censored on the last day known to be alive. Exploratory objectives included collection of translational data regarding the biological effects of the TIL-ACT and its interaction with the TME, using paired tumor biopsies before and after treatment. In particular, tumor samples were collected at screening (if feasible), at surgery (tumor material used for pre-REP), at minimum 30 days after TIL-ACT, after 4 weeks of nivolumab treatment if applicable (optional), and at progression (optional). Detailed list of patients' samples available for translational analysis is provided in fig. S1A. Adverse events were recorded according to NCI Common Terminology Criteria for Adverse Events (v5.0).

Downloaded from https://www.science.org at University of Lausanne on February 05, 2024

Neighborhood mutual interaction analysis, tissue digital reconstruction, and density map

Starting from previously published work (*22*), we elaborated a "mutual interaction" methodology that takes into account "bidirectional" cell-cell interaction.The mutual interaction metric is a way to compute interactions between two species (cells from two different cell types in our case) on a surface (i.e., tumor biopsy microscopy slide). Our total biopsy of area σ can be split into intratumoral regions of area σ_t (defined by the presence of the SOX10 protein marker) and stromal regions of area σ_s (defined by the absence of SOX10) where

$$\sigma = \sigma_t + \sigma_s$$

We can measure the neighboring of a point (i.e., cell) P_A (defined as starting point) of type A (i.e., cell type A) of coordinates x_A, y_A, with type B points (i.e., cells from cell type B; defined as ending points) in the surrounding area with a distance μ (i.e., 20, 45, or 100 μm). The distance between point P_A and a point (i.e., cell) P_B of type B (i.e., cell type B) with coordinates x_B, y_B is then defined as the Euclidean distance d

$$d = \sqrt{(x_A - x_B)^2 + (y_A - y_B)^2}$$

P_B was considered a neighbor of P_A if $d < \mu$. Such definition can be visualized as a circular surrounding of the point P_A with a radius μ.

To define the mutual interaction between a set of points A with size n: $S_A : \{A_1, A_2, A_3, \ldots, A_n\}$ and a set of points B with size m: $S_B : \{B_1, B_2, B_3, \ldots, B_m\}$, we defined the function $F_{\text{neigh}}(A_i, S_B)$ that gives us 1 if there is at least an element of the set B at a distance less or equal than μ for a specific point A_i, otherwise zero.

The mutual interaction, in the total area σ, where there are n cells of type A and m cells of type B, is defined as follows

$$M = \frac{\left(\sum_{i=0}^{i=n} F_{\text{neigh}}(A_i, S_B) + \sum_{i=0}^{i=m} F_{\text{neigh}}(B_i, S_A) \right)}{n + m}$$

The mutual interaction can also be computed in specific area such as intratumoral or stromal regions. For example, mutual interactions between cells of type A in the stroma: $S_{AS} : \{A_1, A_2, A_3, \ldots, A_k\}$ and cells of type B in the stroma: $S_{BS} : \{B_1, B_2, B_3, \ldots, B_o\}$ where there are k cells of type A and o cells of type B is defined as follows

$$M = \frac{\left(\sum_{i=0}^{i=k} F_{\text{neigh}}(A_i, S_B) + \sum_{i=0}^{i=o} F_{\text{neigh}}(B_i, S_A) \right)}{k + o}$$

In such equation where we focused on intratumoral or stromal regions, we still used the entire set S_B (and S_A) because a generic point A_i (or B_i) can be at the edge of its own tissue (stromal or intratumoral, respectively) but could still be a neighbor of type B (or A) in the complementary tissue (intratumoral or stromal, respectively). The mutual interaction metric assumes values between zero and one because, at most, the numerator of the previous formula is $k + o$. The normalizing constant is not introduced simply to scale the values between 0 and 1 but to define a variable that has a biological meaning. Basically, the mutual interaction metric can be interpreted as the relative frequency of interacting cells among all possible cells of both types A and B.

Using precise cell coordinates and phenotypes, we reconstructed the tissues by digitally representing them across the tissue. In particular, to visualize densities of mutual interactions in the digital reconstructed tissue, we used the coordinates of those and a 2D Kernel density estimation (KDE). The KDE allowed us to approximate the density distribution of specific type of niches (or any other kind of species in a 2D surface) and displayed the equiprobability lines for such densities. The higher the number of niches, the higher the overlap was between the equiprobability lines and the actual tissue.

Statistical methods

Statistical analyses were performed as noted in the figure legends using R (version 4.0.3) and SAS (version 9.4) software. In general and unless otherwise mentioned in the legends, statistical significance was assessed by nonparametric test (Wilcoxon rank sum test) when comparing patient data points unless data was log-normalized. Because of the nature of the clinical study and the subsequent low number of patients and low statistical power, no adjustment for multiple comparisons was performed in patient-based analyses. For other analyses involving more data points, like single-cell–based analyses, we used parametric test [Student's t test, analysis of variance (ANOVA), and linear regressions] with multiple comparison adjustment [Bonferroni, post hoc Tukey test, and false discovery rate (FDR), respectively]. All other methods are included in the Supplementary Materials.

Supplementary Materials

This PDF file includes:

Supplemental Methods
Figs. S1 to S7
Legends for data files S1 to S12
References (*41*–*49*)
Supplementary Materials

Other Supplementary Material for this manuscript includes the following:

Data files S1 to S12
MDAR Reproducibility Checklist

REFERENCES AND NOTES

1. U. Dafni, O. Michielin, S. M. Lluesma, Z. Tsourti, V. Polydoropoulou, D. Karlis, M. J. Besser, J. Haanen, I. M. Svane, P. S. Ohashi, U. S. Kammula, A. Orcurto, S. Zimmermann, L. Trueb, C. A. Klebanoff, M. T. Lotze, L. E. Kandalaft, G. Coukos, Efficacy of adoptive therapy with tumor-infiltrating lymphocytes and recombinant interleukin-2 in advanced cutaneous melanoma: A systematic review and meta-analysis. *Ann. Oncol.* **30**, 1902–1913 (2019).
2. M. E. Dudley, J. R. Wunderlich, P. F. Robbins, J. C. Yang, P. Hwu, D. J. Schwartzentruber, S. L. Topalian, R. Sherry, N. P. Restifo, A. M. Hubicki, M. R. Robinson, M. Raffeld, P. Duray, C. A. Seipp, L. Rogers-Freezer, K. E. Morton, S. A. Mavroukakis, D. E. White, S. A. Rosenberg, Cancer regression and autoimmunity in patients after clonal repopulation with antitumor lymphocytes. *Science* **298**, 850–854 (2002).
3. A. A. Sarnaik, O. Hamid, N. I. Khushalani, K. D. Lewis, T. Medina, H. M. Kluger, S. S. Thomas, E. Domingo-Musibay, A. C. Pavlick, E. D. Whitman, S. Martin-Algarra, P. Corrie, B. D. Curti, J. Olah, J. Lutzky, J. S. Weber, J. M. G. Larkin, W. Shi, T. Takamura, M. Jagasia, H. Qin, X. Wu, C. Chartier, F. Graf Finckenstein, M. Fardis, J. M. Kirkwood, J. A. Chesney, Lifileucel, a tumor-infiltrating lymphocyte therapy, in metastatic melanoma. *J. Clin. Oncol.* **39**, 2656–2666 (2021).
4. M. W. Rohaan, T. H. Borch, J. H. van den Berg, O. Met, R. Kessels, M. H. G. Foppen, J. S. Granhoj, B. Nuijen, C. Nijenhuis, I. Jedema, M. van Zon, S. Scheij, J. H. Beijnen, M. Hansen, C. Voermans, I. M. Noringriis, T. J. Monberg, R. B. Holmstroem, L. D. V. Wever, M. van Dijk, L. G. Grijpink-Ongering, L. H. M. Valkenet, A. T. Acosta, M. Karger, J. S. W. Borgers, R. M. T. Ten Ham, V. P. Retel, W. H. van Harten, F. Lalezari, H. van Tinteren, A. A. M. van der Veldt, G. A. P. Hospers, M. A. M. Stevense-den Boer, K. P. M. Suijkerbuijk, M. J. B. Aarts, D. Piersma, A. J. M. van den Eertwegh, J. B. de Groot, G. Vreugdenhil, E. Kapiteijn, M. J. Boers-Sonderen, W. E. Fiets, F. van den Berkmortel, E. Ellebaek, L. R. Holmich, A. C. J. van Akkooi, W. J. van Houdt, M. Wouters, J. V. van Thienen, C. U. Blank, A. Meerveld-Eggink, S. Klobuch, S. Wilgenhof, T. N. Schumacher, M. Donia, I. M. Svane, J. Haanen, Tumor-infiltrating lymphocyte therapy or ipilimumab in advanced melanoma. *N. Engl. J. Med.* **387**, 2113–2125 (2022).
5. G. Coukos, TIL therapy entering the mainstream. *N. Engl. J. Med.* **387**, 2185–2186 (2022).
6. B. C. Creelan, C. Wang, J. K. Teer, E. M. Toloza, J. Yao, S. Kim, A. M. Landin, J. E. Mullinax, J. J. Saller, A. N. Saltos, D. R. Noyes, L. B. Montoya, W. Curry, S. A. Pilon-Thomas, A. A. Chiappori, T. Tanvetyanon, F. J. Kaye, Z. J. Thompson, S. J. Yoder, B. Fang, J. M. Koomen, A. A. Sarnaik, D. T. Chen, J. R. Conejo-Garcia, E. B. Haura, S. J. Antonia, Tumor-infiltrating lymphocyte treatment for anti-PD-1-resistant metastatic lung cancer: A phase 1 trial. *Nat. Med.* **27**, 1410–1418 (2021).
7. S. Stevanovic, S. R. Helman, J. R. Wunderlich, M. M. Langhan, S. L. Doran, M. L. M. Kwong, R. P. T. Somerville, C. A. Klebanoff, U. S. Kammula, R. M. Sherry, J. C. Yang, S. A. Rosenberg, C. S. Hinrichs, A Phase II study of tumor-infiltrating lymphocyte therapy for human papillomavirus-associated epithelial cancers. *Clin. Cancer Res.* **25**, 1486–1493 (2019).
8. N. Zacharakis, H. Chinnasamy, M. Black, H. Xu, Y. C. Lu, Z. Zheng, A. Pasetto, M. Langhan, T. Shelton, T. Prickett, J. Gartner, L. Jia, K. Trebska-McGowan, R. P. Somerville, P. F. Robbins, S. A. Rosenberg, S. L. Goff, S. A. Feldman, Immune recognition of somatic mutations leading to complete durable regression in metastatic breast cancer. *Nat. Med.* **24**, 724–730 (2018).
9. G. Oliveira, K. Stromhaug, S. Klaeger, T. Kula, D. T. Frederick, P. M. Le, J. Forman, T. Huang, S. Li, W. Zhang, Q. Xu, N. Cieri, K. R. Clauser, S. A. Shukla, D. Neuberg, S. Justesen, G. MacBeath, S. A. Carr, E. F. Fritsch, N. Hacohen, M. Sade-Feldman, K. J. Livak, G. M. Boland, P. A. Ott, D. B. Keskin, C. J. Wu, Phenotype, specificity and avidity of antitumour CD8(+) T cells in melanoma. *Nature* **596**, 119–125 (2021).
10. F. J. Lowery, S. Krishna, R. Yossef, N. B. Parikh, P. D. Chatani, N. Zacharakis, M. R. Parkhurst, N. Levin, S. Sindiri, A. Sachs, K. J. Hitscherich, Z. Yu, N. R. Vale, Y. C. Lu, Z. Zheng, L. Jia,

Downloaded from https://www.science.org at University of Lausanne on February 05, 2024

J. J. Gartner, V. K. Hill, A. R. Copeland, S. K. Nah, R. V. Masi, B. Gasmi, S. Kivitz, B. C. Paria, M. Florentin, S. P. Kim, K. I. Hanada, Y. F. Li, L. T. Ngo, S. Ray, M. L. Shindorf, S. T. Levi, R. Shepherd, C. Toy, A. Y. Parikh, T. D. Prickett, M. C. Kelly, R. Beyer, S. L. Goff, J. C. Yang, P. F. Robbins, S. A. Rosenberg, Molecular signatures of antitumor neoantigen-reactive T cells from metastatic human cancers. *Science* **375**, 877–884 (2022).

11. J. R. Veatch, S. M. Lee, C. Shasha, N. Singhi, J. L. Szeto, A. S. Moshiri, T. S. Kim, K. Smythe, P. Kong, M. Fitzgibbon, B. Jesernig, S. Bhatia, S. S. Tykodi, E. T. Hall, D. R. Byrd, J. A. Thompson, V. G. Pillarisetty, T. Duhen, A. McGarry Houghton, E. Newell, R. Gottardo, S. R. Riddell, Neoantigen-specific CD4$^+$ T cells in human melanoma have diverse differentiation states and correlate with CD8$^+$ T cell, macrophage, and B cell function. *Cancer Cell* **40**, 393–409.e9 (2022).
12. P. O. Gannon, A. Harari, A. Auger, C. Murgues, V. Zangiacomi, O. Rubin, K. Ellefsen Lavoie, L. Guillemot, B. Navarro Rodrigo, T. Nguyen-Ngoc, S. Rusakiewicz, L. Rossier, C. Boudousquie, P. Baumgaertner, S. Zimmermann, L. Trueb, E. M. Iancu, C. Sempoux, N. Demartines, G. Coukos, L. E. Kandalaft, Development of an optimized closed and semi-automatic protocol for Good Manufacturing Practice manufacturing of tumor-infiltrating lymphocytes in a hospital environment. *Cytotherapy* **22**, 780–791 (2020).
13. R. Gao, S. Bai, Y. C. Henderson, Y. Lin, A. Schalck, Y. Yan, T. Kumar, M. Hu, E. Sei, A. Davis, F. Wang, S. F. Shaitelman, J. R. Wang, K. Chen, S. Moulder, S. Y. Lai, N. E. Navin, Delineating copy number and clonal substructure in human tumors from single-cell transcriptomes. *Nat. Biotechnol.* **39**, 599–608 (2021).
14. S. Aibar, C. B. Gonzalez-Blas, T. Moerman, V. A. Huynh-Thu, H. Imrichova, G. Hulselmans, F. Rambow, J. C. Marine, P. Geurts, J. Aerts, J. van den Oord, Z. K. Atak, J. Wouters, S. Aerts, SCENIC: Single-cell regulatory network inference and clustering. *Nat. Methods* **14**, 1083–1086 (2017).
15. C. Capparelli, T. J. Purwin, M. Glasheen, S. Caksa, M. Tiago, N. Wilski, D. Pomante, S. Rosenbaum, M. Q. Nguyen, W. Cai, J. Franco-Barraza, R. Zheng, G. Kumar, I. Chervoneva, A. Shimada, V. W. Rebecca, A. E. Snook, K. Hookim, X. Xu, E. Cukierman, M. Herlyn, A. E. Aplin, Targeting SOX10-deficient cells to reduce the dormant-invasive phenotype state in melanoma. *Nat. Commun.* **13**, 1381 (2022).
16. K. E. Yost, A. T. Satpathy, D. K. Wells, Y. Qi, C. Wang, R. Kageyama, K. L. McNamara, J. M. Granja, K. Y. Sarin, R. A. Brown, R. K. Gupta, C. Curtis, S. L. Bucktrout, M. M. Davis, A. L. S. Chang, H. Y. Chang, Clonal replacement of tumor-specific T cells following PD-1 blockade. *Nat. Med.* **25**, 1251–1259 (2019).
17. X. Guo, Y. Zhang, L. Zheng, C. Zheng, J. Song, Q. Zhang, B. Kang, Z. Liu, L. Jin, R. Xing, R. Gao, L. Zhang, M. Dong, X. Hu, X. Ren, D. Kirchhoff, H. G. Roider, T. Yan, Z. Zhang, Global characterization of T cells in non-small-cell lung cancer by single-cell sequencing. *Nat. Med.* **24**, 978–985 (2018).
18. L. Zhang, X. Yu, L. Zheng, Y. Zhang, Y. Li, Q. Fang, R. Gao, B. Kang, Q. Zhang, J. Y. Huang, H. Konno, X. Guo, Y. Ye, S. Gao, S. Wang, X. Hu, X. Ren, Z. Shen, W. Ouyang, Z. Zhang, Lineage tracking reveals dynamic relationships of T cells in colorectal cancer. *Nature* **564**, 268–272 (2018).
19. M. Andreatta, J. Corria-Osorio, S. Muller, R. Cubas, G. Coukos, S. J. Carmona, Interpretation of T cell states from single-cell transcriptomics data using reference atlases. *Nat. Commun.* **12**, 2965 (2021).
20. L. Zheng, S. Qin, W. Si, A. Wang, B. Xing, R. Gao, X. Ren, L. Wang, X. Wu, J. Zhang, N. Wu, N. Zhang, H. Zheng, H. Ouyang, K. Chen, Z. Bu, X. Hu, J. Ji, Z. Zhang, Pan-cancer single-cell landscape of tumor-infiltrating T cells. *Science* **374**, abe6474 (2021).
21. H. Li, A. M. van der Leun, I. Yofe, Y. Lubling, D. Gelbard-Solodkin, A. C. J. van Akkooi, M. van den Braber, E. A. Rozeman, J. Haanen, C. U. Blank, H. M. Horlings, E. David, Y. Baran, A. Bercovich, A. Lifshitz, T. N. Schumacher, A. Tanay, I. Amit, Dysfunctional CD8 T cells form a proliferative, dynamically regulated compartment within human melanoma. *Cell* **176**, 775–789.e18 (2019).
22. J. Duraiswamy, R. Turrini, A. Minasyan, D. Barras, I. Crespo, A. J. Grimm, J. Casado, R. Genolet, F. Benedetti, A. Wicky, K. Ioannidou, W. Castro, C. Neal, A. Moriot, S. Renaud-Tissot, V. Anstett, N. Fahr, J. L. Tanyi, M. A. Eiva, C. A. Jacobson, K. T. Montone, M. C. W. Westergaard, I. M. Svane, L. E. Kandalaft, M. Delorenzi, P. K. Sorger, A. Farkkila, O. Michielin, V. Zoete, S. J. Carmona, P. G. Foukas, D. J. Powell Jr., S. Rusakiewicz, M. A. Doucey, D. Dangaj Laniti, G. Coukos, Myeloid antigen-presenting cell niches sustain antitumor T cells and license PD-1 blockade via CD28 costimulation. *Cancer Cell* **39**, 1623–1642.e20 (2021).
23. D. Dangaj, M. Bruand, A. J. Grimm, C. Ronet, D. Barras, P. A. Duttagupta, E. Lanitis, J. Duraiswamy, J. L. Tanyi, F. Benencia, J. Conejo-Garcia, H. R. Ramay, K. T. Montone, D. J. Powell Jr., P. A. Gimotty, A. Facciabene, D. G. Jackson, J. S. Weber, S. J. Rodig, S. F. Hodi, L. E. Kandalaft, M. Irving, L. Zhang, P. Foukas, S. Rusakiewicz, M. Delorenzi, G. Coukos, Cooperation between constitutive and inducible chemokines enables T cell engraftment and immune attack in solid tumors. *Cancer Cell* **35**, 885–900.e10 (2019).
24. J. Schmidt, J. Chiffelle, M. A. S. Perez, M. Magnin, S. Bobisse, M. Arnaud, R. Genolet, J. Cesbron, D. Barras, B. Navarro Rodrigo, F. Benedetti, A. Michel, L. Queiroz, P. Baumgaertner, P. Guillaume, M. Hebeisen, O. Michielin, T. Nguyen-Ngoc, F. Huber, M. Irving, S. Tissot-Renaud, B. J. Stevenson, S. Rusakiewicz, D. Dangaj Laniti, M. Bassani-Sternberg, N. Rufer, D. Gfeller, L. E. Kandalaft, D. E. Speiser, V. Zoete, G. Coukos, A. Harari, Neoantigen-specific CD8 T cells with high structural avidity preferentially reside in and eliminate tumors. *Nat. Commun.* **14**, 3188 (2023).
25. J. R. Conejo-Garcia, S. Biswas, R. Chaurio, P. C. Rodriguez, Neglected no more: B cell-mediated anti-tumor immunity. *Semin. Immunol.* **65**, 101707 (2023).
26. M. J. Pittet, O. Michielin, D. Migliorini, Clinical relevance of tumour-associated macrophages. *Nat. Rev. Clin. Oncol.* **19**, 402–421 (2022).
27. R. Zilionis, C. Engblom, C. Pfirschke, V. Savova, D. Zemmour, H. D. Saatcioglu, I. Krishnan, G. Maroni, C. V. Meyerovitz, C. M. Kerwin, S. Choi, W. G. Richards, A. De Rienzo, D. G. Tenen, R. Bueno, E. Levantini, M. J. Pittet, A. M. Klein, Single-cell transcriptomics of human and mouse lung cancers reveals conserved myeloid populations across individuals and species. *Immunity* **50**, 1317–1334.e10 (2019).
28. I. Vázquez-García, F. Uhlitz, N. Ceglia, J. L. P. Lim, M. Wu, N. Mohibullah, J. Niyazov, A. E. B. Ruiz, K. M. Boehm, V. Bojilova, C. J. Fong, T. Funnell, D. Grewal, E. Havasov, S. Leung, A. Pasha, D. M. Patel, M. Pourmaleki, N. Rusk, H. Shi, R. Vanguri, M. J. Williams, A. W. Zhang, V. Broach, D. S. Chi, A. D. C. Paula, G. J. Gardner, S. H. Kim, M. Lennon, K. L. Roche, Y. Sonoda, O. Zivanovic, R. Kundra, A. Viale, F. N. Derakhshan, L. Geneslaw, S. I. Bhaloo, A. Maroldi, R. Nunez, F. Pareja, A. Stylianou, M. Vahdatinia, Y. Bykov, R. N. Grisham, Y. L. Liu, Y. Lakhman, I. Nikolovski, D. Kelly, J. Gao, A. Schietinger, T. J. Hollmann, S. F. Bakhoum, R. A. Soslow, L. H. Ellenson, N. R. Abu-Rustum, C. Aghajanian, C. F. Friedman, A. M. Pherson, B. Weigelt, D. Zamarin, S. P. Shah, Ovarian cancer mutational processes drive site-specific immune evasion. *Nature* **612**, 778–786 (2022).
29. M. Kiessler, I. Plesca, U. Sommer, R. Wehner, F. Wilczkowski, L. Muller, A. Tunger, X. Lai, A. Rentsch, K. Peuker, S. Zeissig, A. M. Seifert, L. Seifert, J. Weitz, M. Bachmann, M. Bornhauser, D. Aust, G. Baretton, M. Schmitz, Tumor-infiltrating plasmacytoid dendritic cells are associated with survival in human colon cancer. *J. Immunother. Cancer* **9**, e001813 (2021).
30. L. E. Kandalaft, D. D. Laniti, G. Coukos, Immunobiology of high-grade serous ovarian cancer: Lessons for clinical translation. *Nat. Rev. Cancer* **22**, 640–656 (2022).
31. G. Arbore, E. E. West, J. Rahman, G. Le Friec, N. Niyonzima, M. Pirooznia, I. Tunc, P. Pavlidis, N. Powell, Y. Li, P. Liu, A. Servais, L. Couzi, V. Fremeaux-Bacchi, L. Placais, A. Ferraro, P. R. Walsh, D. Kavanagh, B. Afzali, P. Lavender, H. J. Lachmann, C. Kemper, Complement receptor CD46 co-stimulates optimal human CD8$^+$ T cell effector function via fatty acid metabolism. *Nat. Commun.* **9**, 4186 (2018).
32. M. G. Strainic, J. Liu, D. Huang, F. An, P. N. Lalli, N. Muqim, V. S. Shapiro, G. R. Dubyak, P. S. Heeger, M. E. Medof, Locally produced complement fragments C5a and C3a provide both costimulatory and survival signals to naive CD4$^+$ T cells. *Immunity* **28**, 425–435 (2008).
33. J. M. Wrangle, V. Velcheti, M. R. Patel, E. Garrett-Mayer, E. G. Hill, J. G. Ravenel, J. S. Miller, M. Farhad, K. Anderton, K. Lindsey, M. Taffaro-Neskey, C. Sherman, S. Suriano, M. Swiderska-Syn, A. Sion, J. Harris, A. R. Edwards, J. A. Rytlewski, C. M. Sanders, E. C. Yusko, M. D. Robinson, C. Krieg, W. L. Redmond, J. O. Egan, P. R. Rhode, E. K. Jeng, A. D. Rock, H. C. Wong, M. P. Rubinstein, ALT-803, an IL-15 superagonist, in combination with nivolumab in patients with metastatic non-small cell lung cancer: A non-randomised, open-label, phase 1b trial. *Lancet Oncol.* **19**, 694–704 (2018).
34. A. Giladi, M. Cohen, C. Medaglia, Y. Baran, B. Li, M. Zada, P. Bost, R. Blecher-Gonen, T. M. Salame, J. U. Mayer, E. David, F. Ronchese, A. Tanay, I. Amit, Dissecting cellular crosstalk by sequencing physically interacting cells. *Nat. Biotechnol.* **38**, 629–637 (2020).
35. C. M. Anadon, X. Yu, K. Hanggi, S. Biswas, R. A. Chaurio, A. Martin, K. K. Payne, G. Mandal, P. Innamarato, C. M. Harro, J. A. Mine, K. B. Sprenger, C. Cortina, J. J. Powers, T. L. Costich, B. A. Perez, C. D. Gatenbee, S. Prabhakaran, D. Marchion, M. H. M. Heemskerk, T. J. Curiel, A. R. Anderson, R. M. Wenham, P. C. Rodriguez, J. R. Conejo-Garcia, Ovarian cancer immunogenicity is governed by a narrow subset of progenitor tissue-resident memory T cells. *Cancer Cell* **40**, 545–557.e13 (2022).
36. M. Bruand, D. Barras, M. Mina, E. Ghisoni, M. Morotti, E. Lanitis, N. Fahr, M. Desbuisson, A. Grimm, H. Zhang, C. Chong, J. Dagher, S. Chee, T. Tsianou, J. Dorier, B. J. Stevenson, C. Iseli, C. Ronet, S. Bobisse, R. Genolet, J. Walton, M. Bassani-Sternberg, L. E. Kandalaft, B. Ren, I. McNeish, E. Swisher, A. Harari, M. Delorenzi, G. Ciriello, M. Irving, S. Rusakiewicz, P. G. Foukas, F. Martinon, D. Dangaj Laniti, G. Coukos, Cell-autonomous inflammation of BRCA1-deficient ovarian cancers drives both tumor-intrinsic immunoreactivity and immune resistance via STING. *Cell Rep.* **36**, 109412 (2021).
37. T. F. Gajewski, H. Schreiber, Y. X. Fu, Innate and adaptive immune cells in the tumor microenvironment. *Nat. Immunol.* **14**, 1014–1022 (2013).
38. S. Spranger, D. Dai, B. Horton, T. F. Gajewski, Tumor-Residing Batf3 dendritic cells are required for effector T cell trafficking and adoptive T cell therapy. *Cancer Cell* **31**, 711–723.e4 (2017).
39. I. G. House, P. Savas, J. Lai, A. X. Y. Chen, A. J. Oliver, Z. L. Teo, K. L. Todd, M. A. Henderson, L. Giuffrida, E. V. Petley, K. Sek, S. Mardiana, T. N. Gide, C. Quek, R. A. Scolyer, G. V. Long, J. S. Wilmott, S. Loi, P. K. Darcy, P. A. Beavis, Macrophage-derived CXCL9 and CXCL10 are required for antitumor immune responses following immune checkpoint blockade. *Clin. Cancer Res.* **26**, 487–504 (2020).

Downloaded from https://www.science.org at University of Lausanne on February 05, 2024

40. A. E. Denton, S. Innocentin, E. J. Carr, B. M. Bradford, F. Lafouresse, N. A. Mabbott, U. Morbe, B. Ludewig, J. R. Groom, K. L. Good-Jacobson, M. A. Linterman, Type I interferon induces CXCL13 to support ectopic germinal center formation. *J. Exp. Med.* **216**, 621–637 (2019).
41. J. G. Burel, M. Pomaznoy, C. S. Lindestam Arlehamn, D. Weiskopf, R. da Silva Antunes, Y. Jung, M. Babor, V. Schulten, G. Seumois, J. A. Greenbaum, S. Premawansa, G. Premawansa, A. Wijewickrama, D. Vidanagama, B. Gunasena, R. Tippalagama, A. D. deSilva, R. H. Gilman, M. Saito, R. Taplitz, K. Ley, P. Vijayanand, A. Sette, B. Peters, Circulating T cell-monocyte complexes are markers of immune perturbations. *eLife* **8**, e46045 (2019).
42. T. D. Wu, S. Madireddi, P. E. de Almeida, R. Banchereau, Y. J. Chen, A. S. Chitre, E. Y. Chiang, H. Iftikhar, W. E. O'Gorman, A. Au-Yeung, C. Takahashi, L. D. Goldstein, C. Poon, S. Keerthivasan, D. E. de Almeida Nagata, X. Du, H. M. Lee, K. L. Banta, S. Mariathasan, M. Das Thakur, M. A. Huseni, M. Ballinger, I. Estay, P. Caplazi, Z. Modrusan, L. Delamarre, I. Mellman, R. Bourgon, J. L. Grogan, Peripheral T cell expansion predicts tumour infiltration and clinical response. *Nature* **579**, 274–278 (2020).
43. M. H. Bailey, C. Tokheim, E. Porta-Pardo, S. Sengupta, D. Bertrand, A. Weerasinghe, A. Colaprico, M. C. Wendl, J. Kim, B. Reardon, K.-S. Ng, K. J. Jeong, S. Cao, Z. Wang, J. Gao, Q. Gao, F. Wang, E. M. Liu, L. Mularoni, C. Rubio-Perez, N. Nagarajan, I. Cortes-Ciriano, D. C. Zhou, W. W. Liang, J. M. Hess, V. D. Yellapantula, D. Tamborero, A. Gonzalez-Perez, C. Suphavilai, J. Y. Ko, E. Khurana, P. J. Park, E. M. Van Allen, H. Liang, MC3 Working Group: Cancer Genome Atlas Research Network, M. S. Lawrence, A. Godzik, N. Lopez-Bigas, J. Stuart, D. Wheeler, G. Getz, K. Chen, A. J. Lazar, G. B. Mills, R. Karchin, L. Ding, Comprehensive characterization of cancer driver genes and mutations. *Cell* **173**, 371–385.e318 (2018).
44. L. Jerby-Arnon, P. Shah, M. S. Cuoco, C. Rodman, M. J. Su, J. C. Melms, R. Leeson, A. Kanodia, S. Mei, J. R. Lin, S. Wang, B. Rabasha, D. Liu, G. Zhang, C. Margolais, O. Ashenberg, P. A. Ott, E. I. Buchbinder, R. Haq, F. S. Hodi, G. M. Boland, R. J. Sullivan, D. T. Frederick, B. Miao, T. Moll, K. T. Flaherty, M. Herlyn, R. W. Jenkins, R. Thummalapalli, M. S. Kowalczyk, I. Canadas, B. Schilling, A. N. R. Cartwright, A. M. Luoma, S. Malu, P. Hwu, C. Bernatchez, M. A. Forget, D. A. Barbie, A. K. Shalek, I. Tirosh, P. K. Sorger, K. Wucherpfennig, E. M. Van Allen, D. Schadendorf, B. E. Johnson, A. Rotem, O. Rozenblatt-Rosen, L. A. Garraway, C. H. Yoon, B. Izar, A. Regev, A cancer cell program promotes T cell exclusion and resistance to checkpoint blockade. *Cell* **175**, 984–997.e24 (2018).
45. E. Azizi, A. J. Carr, G. Plitas, A. E. Cornish, C. Konopacki, S. Prabhakaran, J. Nainys, K. Wu, V. Kiseliovas, M. Setty, K. Choi, R. M. Fromme, P. Dao, P. T. McKenney, R. C. Wasti, K. Kadaveru, L. Mazutis, A. Y. Rudensky, D. Pe'er, Single-cell map of diverse immune phenotypes in the breast tumor microenvironment. *Cell* **174**, 1293–1308.e36 (2018).
46. J. Qian, S. Olbrecht, B. Boeckx, H. Vos, D. Laoui, E. Etlioglu, E. Wauters, V. Pomella, S. Verbandt, P. Busschaert, A. Bassez, A. Franken, M. V. Bempt, J. Xiong, B. Weynand, Y. van Herck, A. Antoranz, F. M. Bosisio, B. Thienpont, G. Floris, I. Vergote, A. Smeets, S. Tejpar, D. Lambrechts, A pan-cancer blueprint of the heterogeneous tumor microenvironment revealed by single-cell profiling. *Cell Res.* **30**, 745–762 (2020).
47. Z. Chen, Z. Ji, S. F. Ngiow, S. Manne, Z. Cai, A. C. Huang, J. Johnson, R. P. Staupe, B. Bengsch, C. Xu, S. Yu, M. Kurachi, R. S. Herati, L. A. Vella, A. E. Baxter, J. E. Wu, O. Khan, J.-C. Beltra, J. R. Giles, E. Stelekati, L. M. Mc Lane, C. W. Lau, X. Yang, S. L. Berger, G. Vahedi, H. Ji, E. J. Wherry, TCF-1-centered transcriptional network drives an effector versus exhausted CD8 T cell-fate decision. *Immunity* **51**, 840–855.e5 (2019).
48. M. Hornburg, M. Desbois, S. Lu, Y. Guan, A. A. Lo, S. Kaufman, A. Elrod, A. Lotstein, T. M. DesRochers, J. L. Munoz-Rodriguez, X. Wang, J. Giltnane, O. Mayba, S. J. Turley, R. Bourgon, A. Daemen, Y. Wang, Single-cell dissection of cellular components and interactions shaping the tumor immune phenotypes in ovarian cancer. *Cancer Cell* **39**, 928–944.e6 (2021).
49. V. Thorsson, D. L. Gibbs, S. D. Brown, D. Wolf, D. S. Bortone, T.-H. O. Yang, E. Porta-Pardo, G. Gao, C. L. Plaisier, J. A. Eddy, E. Ziv, A. C. Culhane, E. O. Paull, I. K. A. Sivakumar, A. J. Gentles, R. Malhotra, F. Farshidfar, A. Colaprico, J. S. Parker, L. E. Mose, N. S. Vo, J. Liu, Y. Liu, J. Rader, V. Dhankani, S. M. Reynolds, R. Bowlby, A. Califano, A. D. Cherniack, D. Anastassiou, D. Bedognetti, A. Rao, K. Chen, A. Krasnitz, H. Hu, T. M. Malta, H. Noushmehr, C. S. Pedamallu, S. Bullman, A. I. Ojesina, A. Lamb, W. Zhou, H. Shen, T. K. Choueiri, J. N. Weinstein, J. Guinney, J. Saltz, R. A. Holt, C. E. Rabkin, The Cancer Genome Atlas Research Network, A. J. Lazar, J. S. Serody, E. G. Demicco, M. L. Disis, B. G. Vincent, I. Shmulevich, The immune landscape of cancer. *Immunity* **48**, 812–830.e814 (2018).

Acknowledgments: We are grateful to the patients and patients' families for dedicated collaboration. We thank V. Zimmer, J. Poll, J.-P. Rivals, E. Fortis, A. Benyagoub, and P. Gannon from the Center of Experimental Therapeutics (CTE) Biobank for their assistance. We thank C. Sauvage for assistance with single-cell encapsulation and cDNA library preparations as well as the Agora Flow Cytometry Facility of the University of Lausanne and the Lausanne Genomic Technologies Facility for scRNA-seq/scTCR-seq and RNA-seq analysis. We also apologize to colleagues whose work could not be cited because of space limitations. **Funding:** This study was supported by the Ludwig Institute for Cancer Research, the Swiss Canton of Vaud, Bristol Meyers Squibb, and the following foundations: Biltema, Paul Matson, and Cancera (to G.C.). This study was also supported by the Swiss National Foundation (SNF) R'Equip (316030_205644) (to D.D.L.). **Author contributions:** Conceptualization: D.B., E.G., A.O., S.Z., D.D.L., and G.C. Methodology: D.B., N.F., J.C., S.B., D.L., U.D., A.J.G., M. Morotti, S.T., Z.T., C.A., A.I.K., F. Huber, J.T., I.C., J.C.-O., F.B., R.G., M.P., D.D.L., and G.C. Investigation: D.B., E.G., N.F., J.C., J.D., F.B., I.C., M.B.-S., S.T., D.D.L., and G.C. Visualization: D.B., E.G., J.D., F.B., S.T., and D.D.L. TIL production process: L.E.K. Sample collection and coordination: R. Duran, J.O.P., and L.E.K. Funding acquisition: D.D.L. and G.C. Patient treatments: E.G., A.O., F. Herrera, R. Duran, R. Dummer, M.I., M.O.d.O., B.N., K.H., S.Z., M. Matter, V.A., C.D., N.S., J.O.P., O.M., L.T., and G.B. Supervision: D.D.L., G.C., C.S., A.H., and L.T. Writing—original draft: D.B., E.G., D.D.L., and G.C. Writing—review and editing: D.B., E.G., D.D.L., and G.C. **Competing interests:** In the past 3 years G.C. has received grants and research support or has been coinvestigator in clinical trials by Bristol-Myers Squibb, Tigen Pharma, Iovance, F. Hoffmann-La Roche AG, and Boehringer Ingelheim. The Lausanne University Hospital (CHUV) has received honoraria for advisory services G.C. has provided to Genentech, AstraZeneca AG, and EVIR. Patents related to the NeoTIL technology from the Coukos laboratory have been licensed by the Ludwig Institute, on behalf also of the University of Lausanne and the CHUV, to Tigen Pharma. G.C. has previously received royalties from the University of Pennsylvania for CAR-T cell therapy licensed to Novartis and Tmunity Therapeutics. S.Z. is now an employee of F. Hoffmann-La Roche. R. Duran has intermittent, project-focused consulting and/or advisory relationships with Novartis, Merck Sharp & Dhome (MSD), Bristol-Myers Squibb (BMS), Roche, Amgen, Takeda, Pierre Fabre, Sun Pharma, Sanofi, Catalym, Second Genome, Regeneron, Alligator, T3 Pharma, MaxiVAX SA, Pfizer, and touchIME outside the submitted work. R. Duran has received consulting income from BTG/Boston Scientific, Guerbet, and Medtronic and reports grants from the Society of Interventional Oncology/Immuno-Oncology Research Grant, BTG/Boston Scientific, and Guerbet. O.M. has consulting/advisory roles for Bristol Myers Squibb, MSD, Roche, Novartis, Amgen, Pierre Fabre, and Neracare; has received research grants from Bristol Myers Squibb, MSD, and Amgen; is a consultant advisor or a paid speaker for Bristol Myers Squibb, MSD, Novartis, Pierre Fabre, Amgen, and Nektar; has received research funding from Bristol Myers Squibb and Pierre Fabre; and is the cofounder of a cell therapy company called Cellula. R.G. has received consulting income from Takeda and Ozette Technologies and declares ownership in Ozette Technologies. M.P. has served as a consultant for AstraZeneca, Elstar Therapeutics, ImmuneOncia, KSQ Therapeutics, Merck, Siamab Therapeutics, Third Rock Ventures, and Tidal. U.D. gives expert testimony (personal statistical review and assessment of a clinical trial) for Astra Zeneca and is a member of the Tumor Agnostic Evidence Generation working group for Roche. D.D.L., A.H., and G.C. are inventors on patent applications filed by the Ludwig Institute for Cancer Research Ltd. (US patent application no. 63/281,979) pertaining to the subject matter disclosed herein, and such patent applications have been licensed to Tigen Pharma SA. The other authors declare that they have no competing interest. **Data and materials availability:** All data needed to evaluate the conclusions in the paper are present in the paper or the Supplementary Materials. scRNA-seq, scTCR-seq, and bulk RNA-seq data are available under the NCBI Gene Expression Omnibus (GEO) accession number GSE222448. Spatial GeoMx protein data appears in data file S9.

Submitted 22 January 2023
Accepted 6 December 2023
Published 2 February 2024
10.1126/sciimmunol.adg7995

Downloaded from https://www.science.org at University of Lausanne on February 05, 2024